



## The impact of mineral dust on cloud formation during the Saharan dust event in April 2014 over Europe

Michael Weger<sup>1</sup>, Bernd Heinold<sup>1</sup>, Ina Tegen<sup>1</sup>, Christa Engler<sup>2,3</sup>, Patric Seifert<sup>1</sup>, Holger Baars<sup>1</sup>, Fabian Senf<sup>1</sup>, Corinna Hoose<sup>4</sup>, Romy Ullrich<sup>4</sup>, Axel Seifert<sup>5</sup>, Ulrich Blahak<sup>5</sup>, Martina Krämer<sup>6</sup>, Ulrich Schumann<sup>7</sup>, Christiane Voigt<sup>7,8</sup>, and Stephan Borrmann<sup>8,9</sup>

<sup>1</sup>Leibniz Institute for Tropospheric Research, Leipzig, Germany

<sup>2</sup>Leipzig Institute for Meteorology, University of Leipzig, Leipzig, Germany

<sup>3</sup>Formerly at Leibniz Institute for Tropospheric Research, Leipzig, Germany

<sup>4</sup>Institute of Meteorology and Climate Research, Karlsruhe Institute of Technology, Karlsruhe, Germany

<sup>5</sup>Deutscher Wetterdienst, Offenbach, Germany

<sup>6</sup>Forschungszentrum Jülich, Jülich, Germany

<sup>7</sup>Deutsches Zentrum für Luft- und Raumfahrt, Institut für Physik der Atmosphäre, Oberpfaffenhofen, Germany

<sup>8</sup>Johannes Gutenberg-Universität, Mainz, Germany

<sup>9</sup>Max-Planck-Institut für Chemie, Mainz, Germany

*Correspondence to:* Bernd Heinold

heinold@tropos.de

**Abstract.** A regional modeling study on the impact of desert dust on cloud formation is presented for a major Saharan dust outbreak over Europe from 2 April to 5 April 2014. The dust event coincided with an extensive and dense cirrus cloud layer, suggesting an influence of dust on atmospheric ice nucleation. Using interactive simulation with the regional dust model COSMO-MUSCAT, we investigate cloud and precipitation representation in the model and test the sensitivity of cloud parameters to dust-cloud and dust-radiation interactions of the simulated dust plume. We evaluate model results with ground-based and space-borne remote sensings of aerosol and cloud properties, as well as the in situ measurements obtained during the ML-CIRRUS aircraft campaign. A run of the model with single-moment bulk microphysics without online dust feedback considerably underestimated cirrus cloud cover over Germany in the comparison with infrared satellite imagery. This was also reflected in simulated upper-tropospheric ice water content (IWC), which accounted only for 20 % of the observed values. The interactive dust simulation with COSMO-MUSCAT, including a two-moment bulk microphysics scheme and dust-cloud as well as dust-radiation feedback, in contrast, led to significant improvements. The modeled cirrus cloud cover and IWC were by at least a factor of two higher in the relevant altitudes compared to the non-interactive model run. We attributed these improvements mainly



to enhanced deposition freezing in response to the high mineral dust concentrations. This was corroborated further in a significant decrease in ice particle radii towards more realistic values, as compared to in situ measurements from the ML-CIRRUS aircraft campaign. By testing different empirical ice nucleation parameterizations, we further demonstrate that remaining uncertainties in the ice nucleating properties of mineral dust affect the model performance at least as significantly as to whether including the online representation of the mineral distribution. Dust-radiation interactions played a secondary role for cirrus cloud formation, but contributed to a more realistic representation of precipitation by suppressing moist convection in southern Germany. In addition, a too low specific humidity in the 7 to 10 km altitude range in the boundary conditions was identified as a main reason of misrepresentation of cirrus clouds in this model study.

## 1 Introduction

The Mediterranean and Europe are frequently affected by outbreaks of mineral dust, as specific atmospheric circulation patterns over northern Africa and the Mediterranean cause wind-driven dust emissions over the Sahara and consecutive transport to the north (e.g. Barkan et al., 2005; Salvador et al., 2014). Estimates of annual North African dust emissions range from 400 to 2200 Tg (Huneeus et al., 2011), of which about 10% are exported to Europe (Shao et al., 2011). Mineral dust is an important aerosol constituent (Carslaw et al., 2010), which influences atmospheric processes. The dust particles scatter and absorb solar radiation as well as absorb and re-emit terrestrial radiation (e.g. Müller et al., 2011; Köhler, 2017), which alters the atmospheric stratification and thus can also impact cloud and precipitation formation (Chaboureau et al., 2011; Wang et al., 2013). Moreover, mineral dust particles directly participate in cloud microphysical processes by acting potentially as cloud condensation nuclei (CCN) (Bégue et al., 2015; Karydis et al., 2011) and ice nucleating particles (INP) (DeMott et al., 2003, 2010; Boose et al., 2016).

Based on numerous field and laboratory experiments, a variety of empirical relations to describe the ice nucleating properties of mineral dust for application in numerical weather prediction (NWP) models have been developed so far (e.g. Phillips et al., 2008; Niemand et al., 2012; Hiranuma et al., 2014; DeMott et al., 2015; Ullrich et al., 2017). The impact of dust particles on cloud microphysical and macrophysical properties cannot be generalized as it depends on the cloud type considered, the background aerosol composition, and meteorological conditions. In mixed-phase clouds, mid-tropospheric aerosol entrainment is important to be considered (Fridlind et al., 2004), and additional INPs likely accelerate cloud glaciation, precipitation formation and finally shorten cloud life time (DeMott et al., 2010).



Cirrus clouds either form by lifting of liquid or mixed phase clouds across the homogeneous freezing threshold of 235 K (liquid origin) or in situ by a combination of heterogeneous and homogeneous ice nucleation of super cooled liquid aerosol (in situ origin) (Luebke et al., 2016; Krämer et al., 2016). If homogeneous ice nucleation is primarily involved in the formation of in situ origin cirrus, ice particle concentrations are determined by this process, with a negative correlation between INP concentrations and ice particle concentrations, cloud albedo and emissivity (negative Twomey effect, e.g. Kärcher and Lohmann, 2003). If, however, lifting occurs at low vertical velocities, supersaturation over ice may never exceed the threshold for homogeneous freezing. In this case, ice nucleation is determined by deposition freezing of INPs, with the occurrence of the positive Twomey effect in in situ origin cirrus (Krämer et al., 2016).

As a result of the various atmospheric interaction modes of dust particles, the weather is likely affected by outbreaks of Saharan dust over Europe. It is, e.g., shown by observations that the efficiency of ice formation as well as the ice water content (IWC) are strongly correlated to the presence of mineral dust (Seifert et al., 2010; Zhang et al., 2018; Zhao et al., 2018). Moreover, considering ice nucleation of dust and black carbon in the GCE (Goddard Cumulus Ensemble) model, Lee and Penner (2010) found ice particle number concentrations and ice water path (IWP) increasing with higher INP concentrations for cirrus clouds. Dust particle number concentrations can exceed the hundred fold of the climatological mean value over a wide tropospheric height range during a dust event (Hande et al., 2015). In most operational NWP models, however, aerosol interactions are parameterized using preset aerosol concentrations and characteristics (e.g. The Integrated forecast system (IFS) radiation scheme uses aerosol climatology from Tegen et al. (1997), and cloud droplet and ice particle number concentrations are predefined according to an assumed aerosol background, ECMWF, 2017). Obviously, these models are challenged during those outbreaks and the forecast performance is found to be significantly reduced in the presence of mineral dust (Schumann et al., 2016). In the past, studies with interactive dust modeling approaches were conducted to quantify the effects of desert dust on weather. Smoydzin et al. (2012) included cloud activation and ice nucleation of mineral dust (diagnostically by the DeMott et al. (2010) parameterization) in the coupled chemistry model WRF-chem (Weather Research and Forecasting model – Chemistry) to simulate eastern Mediterranean dust outbreaks. Bangert et al. (2012) used the more detailed ice nucleation scheme by Barahona and Nenes (2009) with INP properties from Phillips et al. (2008) to include the competition of heterogeneous and homogeneous ice nucleation for cirrus cloud formation in their simulations of a major dust outbreak over Europe in 2008 with the regional dust model COSMO-ART (Consortium for Small-scale Modeling – Aerosols and Reactive Trace gases). Both studies found changes in mixed phase cloud microphysics due to mineral dust to



90 various degrees, e.g. more efficient cloud glaciation and a decrease in ice particle radii. Using ICON-ART (Icosahedral Nonhydrostatic – Aerosols and Reactive Trace gases) with a similar setup as Bangert et al. (2012), Rieger et al. (2017) modeled the dust outbreak over Europe in early April 2014 in order to estimate the considerably negative impact of dust-radiation, dust-cloud and combined effects on photovoltaic power generation.

95 The April 2014 Saharan dust outbreak is also the subject of this modeling study. During this event, various cloud systems were present, but most notably, an unusually extensive cirrus canopy occurred. The coincidence of these cloud conditions with the dust plume make it an interesting case to investigate the impact of mineral dust on cloud formation. For the investigation, we use interactive regional dust transport modeling with COSMO-MUSCAT

100 (Consortium for Small-scale Modeling – MULTIScale Chemistry Aerosol Transport) (Wolke et al., 2004, 2012). Particular focus is put on the treatment of heterogeneous ice nucleation of mineral dust. Specifically we investigate: [1] how well cloudiness and precipitation are represented in the COSMO model with the operational radiation and single-moment bulk microphysics parameterizations without considering dust feedback, [2] whether considering

105 dust-cloud and dust-radiation interactions with a two-moment microphysics scheme improves cloud and precipitation representation, and if so, [3] how important is the role of isolated interaction processes therein, and [4] how the choice of the INP-parameterization influences the model results. Based on the answers to these questions, we further seek to improve our understanding of cloud formation during the Saharan mineral dust event. We

110 use a comprehensive observational data set for model evaluation. It consists of standard satellite and ground-based remote sensing, and the unique, rich data set of the campaign ML-CIRRUS (Voigt et al., 2017), consisting of airborne in situ measurements. The present study thus expands the work of Rieger et al. (2017), as it puts the focus on a detailed evaluation of cloud properties during the dust outbreak.

115 The paper is structured as follows: in Section 2, the interactive dust-transport model COSMO-MUSCAT is described together with the setup of sensitivity model runs, and an overview of the observational data available for evaluation is given. Section 3 contains a synoptic overview of the Saharan desert dust outbreak in April 2014. In Section 4, the model results are presented in comparison with the available observational data and a more detailed discussion of the dust impact on cloud microphysics and cloud development is given. Finally,

120 in Section 5 the main outcomes of the study are summarized, followed by the conclusion.





## 2 Methodology

### 2.1 Model description

For the simulations of dust transport and the effects on cloud development, the chemistry transport model MUSCAT (Wolke et al., 2004, 2012) is used, online-coupled to the non-hydrostatic regional NWP model COSMO; version 5.0, of the German Weather Service (DWD) (Doms and Baldauf, 2015).

#### 2.1.1 Operational model configuration

A detailed description of the physical parameterizations applied in the operational version of COSMO can be found in Doms (2008) and Doms et al. (2011). For the treatment of cloud processes and precipitation formation an efficient single-moment bulk water-continuity scheme is used, which considers cloud water, rain, cloud ice, snow, and optionally graupel (not used here) as hydrometeor classes. Conversion processes between these classes, as well as cloud condensation and ice formation are formulated by simple and efficient parameterizations, which do not account explicitly for the impact of a quantifiable aerosol concentration on these processes (i.e. they assume the ubiquitous presence of aerosol particles). As a result, cloud condensation and cloud evaporation is treated by performing saturation adjustment, which is the redistribution of the equivalent amount of water to restore thermodynamic equilibrium between liquid water and water vapour. This approach is reasonable for warm clouds. In mixed phase clouds, however, ice nucleation and ice particle growth occurs outside thermodynamic equilibrium, and both processes are therefore parameterized in more detail in COSMO. The underlying assumption therein is an empirical relationship between the ice particle number concentration  $n_i$  and the temperature  $T$ , which is a fit to aircraft data from Hobbs and Rangno (1985) and Meyers et al. (1992):

$$n_i = 1 \times 10^2 \text{ m}^{-3} \exp[0.2(T - 273.15 \text{ K})]. \quad (1)$$

Equation 1 is used to diagnose  $n_i$  as well as the mean diameter  $D_i$  in the growth equation (e.g. Pruppacher and Klett, 2010) for depositional growth and to deduce an ice nucleation rate for grid cells not containing any cloud ice ( $q_i = 0$ ):

$$\dot{q}_{i,nuc} = \frac{n_i m_i^0}{\rho_{air} \Delta t}. \quad (2)$$

$\dot{q}_{i,nuc}$  is the mass mixing ratio transferred from the water vapor to the ice phase due to heterogeneous ice nucleation per time step  $\Delta t$  and involves the assumption of an initial ice particle mass  $m_i^0 = 1 \times 10^{-12}$  kg.  $\rho_{air}$  is the density of air. Equation 2 is only applied if the



grid cell temperature is lower than the onset temperature for ice formation  $T_{nuc} = 267.15\text{K}$ . Deposition freezing is limited to temperatures lower than  $T_d = 248.15\text{K}$ , whereas for temperatures above  $T_d$ , heterogeneous ice nucleation is the result of condensation freezing, which additionally requires water saturation.

Radiative transfer in COSMO is treated by a  $\delta$ -two-stream scheme, calculating upward and downward shortwave and longwave fluxes in 3 and 5 spectral intervals, respectively (Ritter and Geleyn, 1992). To consider the effects of clouds on radiative transfer, a cloud fraction is parameterized, which encompassed contributions from grid-scale and sub-grid scale stratiform cloudiness as well as convective cloudiness. Accordingly, modified liquid and ice water mixing ratios ( $q_{sc,c}$  and  $q_{sc,i}$ ), containing the sub-grid scale contributions, are derived, which are used to calculate optical properties of clouds. Most importantly, the generalized effective diameter  $D^{ef}$  is directly related to  $q_{sc,c/i}$  via empirical formulations. Radiative transfer further depends on the vertical alignment of cloud free and cloud covered areas in adjacent layers. It is assumed that clouds have maximum overlap, unless there is an intermediate layer without any cloudiness. In this case clouds are distributed randomly. To include the effects of aerosols, a spatially variable climatological mean aerosol distribution is prescribed, with consideration of 5 different types of aerosol optical properties (maritime, continental, urban, volcanic and background stratospheric).

### 2.1.2 Dust scheme

Dust emission and transport are computed by the multiscale transport model MUSCAT, including the parameterization of dust emission and deposition fluxes is given in Heinold et al. (2007), Heinold et al. (2011) and Schepanski et al. (2017). Mineral dust is transported as a passive tracer in five size bins with the particle diameter limits at  $0.2\ \mu\text{m}$ ,  $0.6\ \mu\text{m}$ ,  $1.8\ \mu\text{m}$ ,  $5.2\ \mu\text{m}$ ,  $16\ \mu\text{m}$  and  $48\ \mu\text{m}$ . For dust advection, in MUSCAT, a third-order upstream scheme is used along with an implicit–explicit integration scheme (Knoth and Wolke, 1998; Wolke et al., 2000). The dust source scheme is based on the work of Tegen et al. (2002) and includes the parameterization of the threshold friction velocity  $u_t^*$  for particle mobilization.  $u_t^*$  is dependent on the soil particle size distribution (Marticorena and Bergametti, 1995), which is resolved in four size classes (coarse sand, medium/fine sand, silt and clay) and the surface roughness length  $z_0$ . To account for the effect of vegetation on dust emission, 27 different vegetation types are considered. Vegetation cover is further parameterized according to Knorr and Heimann (1995), using satellite based normalized difference vegetation index (NDVI) data sets (Tucker et al., 2005). Based on the vegetation type and cover as well as snow cover, an effective area  $A^{ef}$  for dust emission is calculated. Soil moisture content, derived from the hydrological fields of COSMO, is assumed to suppress dust emission, if exceeding 99%. The frictional velocity  $u_*$  is calculated from COSMO first layer winds us-



ing surface roughness data from satellite retrievals (Prigent et al., 2012). If  $u_* > u_t^*$ , dust  
190 emission is allowed and computed with a cubic function of  $u_*$  (Heinold et al., 2007). The  
potential areas of dust emission are prescribed using a dust source activation frequency  
mask. This is derived from Meteosat Second Generation (MSG) Spinning Spinning En-  
hanced Visible and InfraRed Imager (SEVIRI) dust index observations (Schepanski et al.,  
2017). Dust removal is treated as dry (Zhang et al., 2001) and wet deposition, while the  
195 latter considers in-cloud and below cloud scavenging (Berge, 1993; Jacobson, 1997; Jonson  
et al., 1998).

Comparisons with results from field studies show that the model provides a good repre-  
sentation of the different aspects of the atmospheric dust cycle (e.g. Heinold et al., 2011).

### 2.1.3 Dust-cloud interactions

200 For the interaction of simulated dust with clouds, the two-moment bulk microphysics  
scheme of Seifert and Beheng (2006) as also implemented in COSMO was modified to in-  
clude the effects of a variable mineral dust concentration on cloud activation and hetero-  
geneous ice nucleation. In past modeling studies, it was commonly assumed for in-cloud  
conditions that all aerosol particles are scavenged by the cloud droplets (e.g., Bangert et al.,  
205 2011). As a consequence, cloud freezing had to be treated stochastically only depending on  
cloud droplet number concentrations but not on a variable aerosol concentrations (Bangert  
et al., 2012). Field studies, however, have shown the assumption of complete in-cloud scav-  
enging is usually violated, especially toward the cloud edges (Gillani et al., 1995) or in the  
presence of ice particles (Verheggen et al., 2007). In this work, for a detailed description  
210 of in-cloud droplet activation as well as ice nucleation (immersion, contact and deposi-  
tion nucleation), the aerosol concentration  $n_a$  is partitioned into an interstitial  $n_{in}$  and by  
cloud water scavenged component  $n_{sc}$ . Aerosol species considered are mineral dust, soot  
and organics, while the latter are given by prescribed number concentrations (see Tab. 2).  
The cloud number concentration  $n_c$  is used to determine  $n_{sc}$ , and accordingly if  $n_c > n_a$ ,  
215  $n_{sc} = n_a$ , otherwise  $n_{sc} = n_c$ . In latter case, the 5 particle size classes are partitioned by  
applying weighting factors based on data of a case study report by Hallberg et al. (1994),  
which prioritize the larger particle classes.

Cloud droplet activation is parameterized according to AbdulRazzak and Ghan (2000) for  
a multi-mode aerosol, consisting of different size classes and different chemical groups.

220 The different chemical composition of dust, soot and organics is represented by different  
hygroscopicity parameters  $\kappa$ . We use the following set of hygroscopicity parameters for  
dust, soot and organics: 0.14, 0.308, 0.308, respectively. The parameterization was origi-  
nally developed for droplet activation at the cloud base, considering the competition of  
the different aerosol modes in an ascending air parcel. To modify the parameterization for



225 in-cloud conditions, preexisting cloud droplets are considered as an additional competing aerosol mode with the size being the mean droplet diameter  $D_c$  and with  $\kappa \approx 0$ . Consequently, only the interstitial aerosol component is available for droplet activation.

Heterogeneous ice nucleation in our model is based on empirical parameterizations of the aerosol surface density of ice nucleation active sites (INAS)  $n_{IS}$  [ $\mu\text{m}^{-2}$ ], presuming the validity of the singular hypothesis. For desert dust, we use the parameterization of Ullrich et al. (2017) as default, which can be considered as one of the most accurate to date. It is based on a comprehensive data set gathered by nucleation experiments, carried out in the Aerosol Interaction and Dynamics in the Atmosphere (AIDA) facility (Wagner et al., 2006), and a novel algorithm for data evaluation. It is supposed to be an especially reliable parameterization for deposition nucleation as it shows the characteristic u-shape of INAS-density isolines, which is in accordance with more recent theoretical work on deposition nucleation (Marcolli, 2014). For soot and organics, we use the parameterization of Phillips et al. (2008), which is based on field studies.

235 Heterogeneous cloud droplet freezing is determined by the probability  $P_{fr}$  for a single cloud droplet to freeze, hence after evolution of model time step  $\Delta t$ , the number of heterogeneously frozen droplets is:

$$\Delta n_{c,het} = -n_c P_{fr}. \quad (3)$$

$P_{fr}$  results from the combined probabilities for immersion ( $P_{im}$ ) and contact freezing ( $P_{co}$ ):

$$P_{fr} = 1 - (1 - P_{im})(1 - P_{co}). \quad (4)$$

245 In a first order approximation,  $P_{co}$  is proportional to the number of colliding interstitial aerosol particles with cloud droplets during evolution of model time step  $\Delta t$ . To parameterize the collision rate, the collision kernel  $\Psi_{co}^l$  of Ovtchinnikov and Kogan (2000) is used, which includes the attractive or repulsive forces of Brownian motion, thermophoresis and diffusiophoresis. It depends on the diameter of colliding particles, approximated here as the first moment of the cloud droplet PSD and the mean diameter of considered aerosol particle size bin  $l$ . In Eq. 5, it is summed over all aerosol indices for chemical class  $k$  and size  $l$ .

$$P_{co} = \sum_{k,l} n_{in}^{k,l} \Psi_{co}^l P_{IN}^{k,l} \Delta t. \quad (5)$$

255  $P_{im}$  results from immersed potential INPs, which activate if the temperature tendency  $\Delta T = T(t + \Delta t) - T(t)$  is negative, which leads to a temporal increase in INP concentra-



tions.  $\Delta T$  is diagnosed using the grid-scale vertical velocity  $w$  and the vertical temperature gradient  $dT/dz$ , thus neglecting horizontal temperature advection. Only the scavenged aerosol component  $n_{sc}$  is available for immersion freezing:

$$260 \quad P_{im} = \frac{1}{n_c} \sum_{k,l} n_{sc}^{k,l} \Delta P_{IN}^{k,l}(T, \Delta T_t), \quad (6)$$

Both Eq. 5 and 6 contain the probability  $P_{IN}$  of an aerosol particle to act as an INP, which is based on a Poisson distribution:

$$P_{IN}^{k,l}(T) = 1 - \exp \{ -n_{IS} [T, S_i^w(T)] \omega^{k,l} \}. \quad (7)$$

Therein the expectation value refers to the mean number of INAS per particle being active at temperature  $T$  and saturation over ice  $S_i$ .  $\omega^{k,l}$  is the mean aerosol surface, of the considered aerosol mode. For contact and immersion freezing,  $n_{IS}$  is evaluated at water saturation, as indicated by  $S_i = S_i^w(T)$ . The freezing threshold for contact freezing was found to be about 4.5 K higher than for immersion freezing (Shaw et al., 2005), thus in the case of contact freezing a correction term  $\Delta T_{co} = 4.5 \text{ K}$  is applied in the calculation of  $n_{IS}$ .

270 For contact freezing, colliding aerosol particles are represented by a population of completely inactivated aerosol particles. For immersion freezing, however, the fraction of already frozen INPs needs to be taken into account by calculating the increase of  $P_{IN}$  during  $\Delta t$ :

$$\Delta P_{IN}(T, \Delta T_t) = \text{Max} [0, P_{IN}(T + \Delta T) - P_{IN}(T)]. \quad (8)$$

275 Deposition freezing of water vapour on interstitial aerosol particles predominantly takes place in pure ice clouds at  $S_i > 1$  and  $T < 235 \text{ K}$ . These restrictions are not explicitly made here, as the empirical INP-parameterizations for deposition freezing are also valid for higher temperatures. In most cases, however, cloud droplet freezing and deposition nucleation are not expected to occur simultaneously at significant rates, as at water saturation and for  $T > 235 \text{ K}$  deposition nucleation is not efficient. The number of newly nucleated ice particles in the deposition freezing mode  $\Delta n_{i,dep}$  is calculated diagnostically according to Seifert and Beheng (2006), as a balance equation for interstitial aerosol would be needed for a prognostical treatment (in opposition to cloud droplet freezing, where there is a balance equation for  $n_c$ ). Thus,  $\Delta n_{i,dep}$  is limited by the ice and snow particle number concentrations  $n_i$  and  $n_s$ , respectively:

285

$$\Delta n_{i,dep} = \text{Max}(0, \sum_{k,l} n_{in}^{k,l} P_{IN}^{k,l} - n_i - n_s). \quad (9)$$



Finally, the number of heterogeneously frozen ice crystals due to ice nucleation  $\Delta n_{i,het}$  is given as the sum of heterogeneous cloud droplet freezing and deposition freezing:

$$\Delta n_{i,het} = -\Delta n_{c,het} + \Delta n_{i,dep} \quad (10)$$

290 Homogeneous freezing of cloud droplets is treated as in Seifert and Beheng (2006), with a stochastic approach and a temperature dependent freezing rate constant (Cotton and Field, 2002).

#### 2.1.4 Dust-radiation interactions

The computation of short- and longwave radiative fluxes in COSMO considers scattering,  
295 absorption and re-emission by aerosols, cloud hydrometeors and trace gases. In interactive COSMO-MUSCAT simulations, it additionally takes into account the modeled size-resolved dust distribution (Helmert et al., 2007). The model thus considers the direct radiative impact and related dynamical feedbacks of the spatially and temporally varying atmospheric dust load. Dust optical thickness is calculated based on the modeled dust  
300 concentration by assuming spherical particles. The optical properties of Saharan dust are derived from Mie theory (Mishchenko et al., 2002) using refractive indices from Sinyuk et al. (2003).

In order to make use of the more detailed two-moment microphysics information, the single-moment microphysics approach of parameterizing cloud optical properties in Rit-  
305 ter and Geleyn (1992) was revised by Dipu et al. (2017). This way also the impact of the spatially and temporally varying size of cloud droplets and ice crystals on cloud optical depth and reflectivity is accounted for, by using the prognostic version of the effective diameter  $D_i^{ef}$  of cloud droplets and ice crystals. For cloud ice,  $D_i^{ef}$  is defined by:

$$D_i^{ef} = \frac{3IWC}{2\rho_i\sigma_i} \quad (11)$$

310 (e.g. Mitchell et al., 2011), with the specific mass of ice  $\rho_i$ , the water content IWC and the mean particle cross-section  $\sigma_i$ . Assuming shape parameters for ice particles, IWC and  $\sigma_i$  are directly computed from the prognostic variables  $n_i$  and  $q_i$  (and similarly for cloud water content LWC from  $n_c$  and  $q_c$ ), which should lead to a much more accurate representation of dust-cloud-radiation effects in the model.

#### 315 2.2 Simulation setup

COSMO-MUSCAT is applied on two-fold nested domains, as depicted in Fig. 1, to simulate the Saharan dust outbreak in early April 2014 over Europe. The outer domain D1,



which covers Europe and North Africa provides the emission and long-range transport of Saharan dust toward Europe, while the inner domain D2 is used for investigating the representation of cloudiness and precipitation over Germany. Domain D1 has a horizontal resolution of 14 km, is divided into 40 vertical layers up to an altitude of 20 km, and spans the area enclosed within 20° N, 20° W and 61.5° N, 39° E. In this simulation, COSMO is run with the operational single-moment bulk water continuity microphysics scheme and without dust-cloud interactions. However, interactive dust-radiation interactions according to Heinold et al. (2007) were considered. A Tiedtke (Tiedke,1989) convection scheme was used to treat sub-grid scale cloud and precipitation processes, related to moist convection, as horizontal resolution is not sufficient to explicitly resolve these processes. The dust simulation is run for the period 27 March to 6 April, in order to cover associated dust emissions and the development and evolution of the dust plume. COSMO is driven by initial and boundary fields from analysis of the global GME model of DWD. The simulations are re-initialised every 48 h to keep the model meteorology close to the real synoptic situation. One cycle consists of 24 h of meteorological simulation, followed by another 24 h of COSMO-MUSCAT dust simulation. This allows enough relaxation time for the meteorological fields after re-initialization, as only the second half of the cycle is evaluated. The dust distribution of the previous run is used to initialize the following, respectively. The dependency of dust emission on surface winds is highly non-linear. The modeled dust is therefore highly sensitive to uncertainties in surface and soil properties as well as predicted wind speed. In order to match satellite and ground based observations of dust optical thickness, the threshold velocity for dust mobilization is reduced by a factor of 0.63.

For the simulation of dust-cloud interactions over central Europe, COSMO-MUSCAT is run on the inner domain D2 with 2.8 km resolution and with 50 vertical layers. The area spans the coordinate range enclosed within 48.3° N, 4.0° E and 55.3° N, 13.0° E. The simulation is started on 3 April 2014, 00:00 UTC and run for 60 hours without restart. COSMO is initialised and driven with hourly analysis data from the operational COSMO-DE run provided by DWD in order to use driving conditions that are closest to the actual weather situation and benefit from the finer grid spacing. The simulated dust fields of D1 are interpolated onto the D2 grid and used for initialisation of the dust fields of D2, as well as for the 6-hourly updated lateral boundary conditions. As the model-domain resolution permits moist deep convection, the Tiedtke scheme is restricted to parameterize shallow convection only.

One D2 model run is performed with the single-moment bulk microphysics scheme as for D1. To ensure numerical stability of the microphysics schemes, the model integration time step is lowered to 10 s compared to the 25 s standard. Model evaluation is started after a





**Table 1.** Overview of the model runs performed in this study to investigate dust-cloud interactions (DCI) and dust-radiation interactions (DRI). CLM denotes the spatially and temporally fixed climatological mean dust concentration, INT indicates the interactively simulated dust concentration. U17 refers to the parameterization of Ullrich et al. (2017), and P08 to the parameterization of Phillips et al. (2008)

Run	Purpose	Dust INAS density	Dust INP	Dust CCN	Dust radiation
<b>SMBLK</b>	Reference, without DCI and RCI	-	-	-	-
<b>ICLM</b>	DCI and DRI at normal low dust conditions	U17	CLM	CLM	CLM
<b>IINT</b>	DCI and DRI of simulated dust outbreak	U17	INT	INT	INT
<b>RCLM</b>	Evaluate DRI of climatological dust	U17	INT	INT	CLM
<b>CCLM</b>	Evaluate CCN-effect of climatological dust	U17	INT	CLM	INT
<b>IAIP</b>	Test alternative ice parameterization for dust	P08	INT	INT	INT

355 model spin-up time of 24 h on 4 April 2014, 00:00 UTC, which roughly coincides with the appearance of the dense cirrus canopy over Germany in the satellite images.

**Table 2.** Aerosol size distribution for dust, soot and organics used in COSMO-MUSCAT for the climatological mean background. The number concentrations for dust are based on the temporal and spatial mean of simulated dust fields of a model run carried out on domain D2. The values for soot and organics are taken from Phillips et al. (2008), and accredited to the smallest size bin. The size bins are distributed logarithmically with a relative standard deviation of  $\sigma = 2$ .

size bin	mean volume diameter [ $\mu\text{m}$ ]	number concentration [ $\text{m}^{-3}$ ]		
		dust	soot	organics
1	0.39	$1.10 \times 10^5$	$1.50 \times 10^7$	$1.77 \times 10^8$
2	1.17	$5.02 \times 10^4$	-	-
3	3.53	$2.00 \times 10^3$	-	-
4	10.65	$2.18 \times 10^2$	-	-
5	32.16	$2.36 \times 10^{-6}$	-	-

To evaluate the effects of the dust plume on cloud activation, ice nucleation and radiation, four additional model runs are carried out on D2, deploying the two-moment scheme by Seifert and Beheng (2006) with the modifications to allow for the online feedback of  
 360 dust on cloud activation and ice nucleation. For ice nucleation of desert dust, the most up-



to-date INAS density parameterization of Ullrich et al. (2017) (U17) is chosen as default, while for the climatological background aerosol of soot and organics we rely on the parameterization of Phillips et al. (2008) (P08). A summary of the sensitivity model runs is given in Tab. 1, and parameters of the climatological mean aerosol particle size distribution  
365 (PSD) are listed in Tab. 2. The run ICLM is used to represent a climatological background dust scenario with two-moment microphysics, while IINT uses the simulated dust fields instead of the constant prescribed dust PSD. In RCLM and CCLM dust-radiation and dust-cloud-activation are computed using the prescribed climatological mean dust concentration (modeled dust PSD, but with dust amount reduced to spatially uniform low average  
370 value), respectively, in order to disentangle those effects of the simulated dust plume from the fully interactive effects seen in IINT. Finally IAIP is analogous to IINT, but uses the parameterization of P08 for ice nucleation of mineral dust.

## 2.3 Observational data

### 2.3.1 Cloud radar observations

375 To evaluate the modeled IWC, 94 GHz spaceborne and 35 GHz ground-based cloud radar observations are used. From the model side, the contributions from the mixing ratios of cloud ice ( $q_i$ ), snow ( $q_s$ ), graupel ( $q_g$ ), as well as the sub-grid scale ice ( $q_{i,sc}$ ) have to be included.  $q_{i,sc}$  is parameterized with a relative humidity scheme and the stratiform cloud fraction. By using the density of air, the values are converted to units [ $\text{g m}^{-3}$ ].

380 Observational data comprise a vertical cross section of IWC along a CloudSat satellite overpass on 4 April, 12:30 UTC (granules: 12457-42209) with an along-track resolution of 1.7 km (data product 2B-CWC-RO P\_R04, Austin et al., 2009). To compare these data to model results, overflowed grid cells are extracted from the D2 domain and observations are interpolated onto this array. Furthermore, vertical coordinate transformation to the 51 layer  
385 boundary heights of COSMO-MUSCAT is carried out, by averaging over all observations located within the corresponding model layer. Finally, horizontal grid-cell averages are computed for both observational and model data.

In addition to the CloudSat profile, a time series of vertical profiles of IWC retrieved from the 35 GHz zenith pointing radar at Leibniz Institute for Tropospheric Research (TROPOS)  
390 (51.3° N, 12.3° E) is available. The cloud radar of type Mira-35 (Görsdorf et al., 2015) is operated within the Leipzig Aerosol and Cloud Observations System (LACROS, Bühl et al., 2013) which comprises in addition an extensive set of active and passive ground-based remote sensing instrumentation, such as lidar (PollyXT, Engelmann et al., 2016), Microwave radiometer (HATPRO, Rose et al., 2005) and optical disdrometer. The observations  
395 of LACROS are automatically processed within Cloudnet (Illingworth et al., 2007) based



on which a hydrometeor and aerosol target categorization is derived. Cloudnet provides output with a temporal and vertical resolution of 30 s and 30 m, respectively. The Cloudnet target classification builds the basis for the retrieval of products such as liquid water content and ice water content. The ice water content is derived for all identified ice-only  
400 measurement points based on a parameterization of Hogan et al. (2006) that uses an empirical relationship between ice water content, temperature, and radar reflectivity factor. In order to compare these data to equivalent model results, in a first step the original data set is averaged over variable time periods around the dates of the model output with 15 min intervals. The number of measurements to include in a single averaging procedure is given  
405 by horizontal advection and is therefore calculated based on the horizontal grid spacing of 2.8 km and the modeled horizontal wind speed. After vertical coordinate transformation, the obtained data sets are time averaged over the period from 4 April, 00:00 UTC to 5 April, 12:00 UTC.

### 2.3.2 Infrared satellite imagery

410 Model output fields of the hydrometeor mixing ratios, as well as thermodynamic variables are supplied to an infrared (IR) forward simulation (see Appendix A for a detailed description). Resulting synthetic infrared images can be compared to satellite images obtained with the Spinning Enhanced Visible and Infrared Imager (SEVIRI) instrument aboard Meteosat Second Generation (MSG) satellite and provided by EUMETSAT (<https://www.eumetsat.int>). For the atmospheric window channel at 8.7  $\mu\text{m}$ , brightness temperature is used as a proxy for cloud top temperature of optically dense clouds, and further as a measure of cloud top height.  
415

### 2.3.3 Precipitation records

For Germany and closely surrounding areas, hourly precipitation totals are available for a  
420 total of 970 stations. The data is provided by the Climate Data Center (CDC) of the German weather service DWD (<http://www.dwd.de/cdc>). The data was integrated over the model evaluation period from 4 April 2014, 00:00 UTC to 5 April 2014, 12:00 UTC and is used to evaluate the modeled precipitation amount for the different model runs.

### 2.3.4 ML-CIRRUS cloud microphysical measurements

425 During the ML-CIRRUS campaign (Voigt et al., 2017), 16 flights were performed from 26 March to 15 April 2014 with the High Altitude and Long Range Research Aircraft (HALO). The campaign had the scope to investigate cirrus and contrail cirrus above Germany and Western Europe with a novel in situ and remote sensing payload. For model evaluation, the flights conducted on 3 and 4 April provide valuable information on cloud microphysical



430 and thermodynamic properties.

Cloud particle number concentrations for 3 April were measured with the particle spectrometer NIXE-CAPS (Baumgardner et al., 2001; Meyer, 2013), which consists of the cloud and aerosol spectrometer NIXE-CAS to measure size and concentration of particles in the diameter range between 0.61  $\mu\text{m}$  to 50  $\mu\text{m}$ , and the optical particle counter NIXE-CIP to  
435 measure particles in the diameter range of 15  $\mu\text{m}$  to 945  $\mu\text{m}$  with 15  $\mu\text{m}$  resolution. On 4 April, data were not available for the NIXE-CIP instrument. For particle diameters larger than 25  $\mu\text{m}$ , we therefore used available measurements from the Cloud Combination Probe (CCP) CIP instrument (Weigel et al., 2016). To limit aerosol contamination, we do not consider size bins containing particles smaller than 3  $\mu\text{m}$ . PSD of ice particles in the form  
440 of particle number concentration density [ $\text{m}^{-3}\mu\text{m}^{-1}$ ], if not yet calculated, is simply approximated by dividing absolute particle counts in the sample volume of  $10^{-6}\text{m}^3$ , by the diameter range of each size bin. According to the aircraft altitude, measurements were assigned to the corresponding vertical layer of COSMO-MUSCAT on D2. For each layer the horizontally averaged PSD was calculated. Measurements with non-significant particle  
445 concentrations ( $n_i < 1\text{m}^{-3}$ ) were not considered. IWC was retrieved from the measured PSD, assuming empirical mass-diameter relationships according to Krämer et al. (2016) and using the arithmetic mean of the size bin limits. For a measurement, the sphere-equivalent mean diameter  $D_i$  can be obtained simply by:

$$D_i = \left( \frac{\text{IWC}}{n_i \rho_i} \right)^{\frac{1}{3}}. \quad (12)$$

450 The number-averaged diameter  $\bar{D}_N$  of an ensemble of measurements is then defined by:

$$\bar{D}_N = \sum D_i n_i / \sum n_i, \quad (13)$$

and similarly the IWC-averaged  $\bar{D}_{\text{IWC}}$  by:

$$\bar{D}_{\text{IWC}} = \sum D_i \text{IWC} / \sum \text{IWC}. \quad (14)$$

To find comparable model data, for each HALO measurement a horizontal circle with  
455 radius  $r = 100\text{km}$  around the aircraft position is defined. The selection of this radius is justified, when considering the large impact of randomness on the distribution of clouds in the model at this length-scale. Within this circle and at the model layer in which the aircraft is situated, the closest grid cell to the aircraft position is taken, which further has a grid-cell average IWC value in the same order of magnitude than that of the respective measurement.  
460 For the comparison of IWC, both measured, as well as modeled IWC, containing



contributions from  $q_i$  and  $q_s$ , are discretized in 9 levels. If there is no grid cell meeting this criterion, the respective measurement is excluded from a direct comparison with model results. By this approach, the co-dependence of  $D_i$  on IWC is taken into account, as well as to some extent the geographical co-dependence, which increases the significance of the comparison. For different model runs, however, the resulting number of data pairs can be different, as clouds are differently distributed in the model runs. For the ML-CIRRUS flight on 4 April, this approach cannot be applied, as the HALO flight-track is located completely outside of the domain D2. Nevertheless, these observations are useful for comparison with data from the ML-CIRRUS flight conducted on 3 April.

#### 470 2.3.5 Atmospheric soundings

To evaluate the thermodynamic state of the atmosphere in the model, 12 or 6 hourly datasets of atmospheric soundings (source: University of Wyoming; <http://weather.uwyo.edu/upperair/sounding.html>) are used from the stations Essen (51.40° N, 6.97° E), Norderney (53.71° N, 7.15° E), Schleswig (54.53° N, 9.55° E), Greifswald (54.10° N, 13.40° E), Bergen (52.81° N, 9.93° E), Lindenberg (52.21° N, 14.12° E), Kümmersbruck (49.43° N, 11.90° E), Meiningen (50.56° N, 10.38° E) and Idar-Oberstein (49.70° N, 7.33° E). For evaluation of the model results, vertical profiles of specific humidity are used, which is regarded as the main limiting factor for ice formation. For the dates 4 April, 00:00 UTC, 4 April, 12:00 UTC and 5 April, 00:00 UTC, vertical profiles of specific humidity for the aforementioned stations were averaged. This data set can be directly compared to corresponding model data extracted at the closest geographical positions to the stations.

#### 2.3.6 Dust aerosol observations

For dust model evaluation, a comprehensive set of Aerosol Robotic Network (AERONET) (<https://aeronet.gsfc.nasa.gov>, Holben et al., 1998) sun photometer observations of aerosol optical depth (AOD) are used. Measurement sites are located in northern Africa and Europe, with a total of 40 available stations over the simulation period. While sun photometer measurements are affected by all types of aerosol, COSMO-MUSCAT AODs only consider dust. However, the coarse mode AOD product (level 2.0 quality) of AERONET (O'Neill et al., 2003) predominantly represents the dust fraction and is thus commonly used for evaluating dust only model results. In addition to the AERONET observations, a particle extinction coefficient profile, retrieved from lidar measurements (Baars et al., 2016) at TROPOS in Leipzig is used to evaluate the modeled vertical mineral dust distribution over Europe. Therefore, modeled mass extinction coefficients are derived from the dust PSDs by using refractive indices of Sinyuk et al. (2003) applying Mie theory. With further vertical integration of the mass extinction coefficients, dust AOD values are obtained for comparison



with AERONET data.

### 3 Dust outbreak April 2014

In early April 2014, a pronounced trough of low pressure was situated over the eastern Atlantic Ocean, placing western Europe under a recurrent southerly flow pattern. On 2 April, the trough propagated eastward with the associated cold front reaching the Atlas Mountains at the Moroccan/Algerian border, where it initiated a small lee cyclone to the south of the mountain range. Consecutively, high surface winds caused large dust emissions in the afternoon on 2 April. Figure 2a shows the MSG IR false color dust index indicating dust presence by magenta and purple colored shadings. In addition, isolines of 500 hPa geopotential height illustrate the synoptic situation at this time. The associated intense dust plume can be clearly identified from the magenta coloring over the Moroccan/Algerian border. Furthermore, the 500 hPa geopotential height contour lines indicate air mass transport toward the western Mediterranean basin. Inside the conveyor belt, which closely goes ahead of the cold front, strong lifting caused the Saharan dust eventually to reach the upper troposphere, where it was further transported eastward behind the pronounced ridge axis. Based on this analysis, a destination of the lifted dust over western and central Europe can be expected.

Over the consecutive day, the eastward travelling cold front caused nearly continuous dust emissions (albeit weaker than the event in the afternoon on 2 April) over the desert in Algeria and Tunisia (see purple features in Fig. 2b). The persistence of the aforementioned flow pattern also favored most of this dust eventually reaching Europe on 3 April. With the development of an upper level cut-off low over the western Mediterranean Sea and with its eastward movement, upper level winds over south-central Europe became more and more easterly on 4 April and as a consequence, dust export from North Africa to central Europe was not further supported. Ongoing upper level lifting, especially at the northern boundary of the advancing Saharan mineral dust-rich airmas caused the development of extensive cirrus cloudiness. The horizontal extension as well as the high optical density of the cirrus shield became striking in the morning hours of 4 April, as associated cloud top temperatures reached below 210 K over a large area, covering parts of France, Great Britain, the Benelux States, and Germany (see Fig. 2c). A link of the high atmospheric mineral dust concentrations to this cloud development seems likely, as desert dust has excellent ice nucleating abilities and furthermore it can destabilize the thermodynamic stratification of the atmosphere at the upper edge of the dust plume through interaction with radiation. Weak anticyclonic currents over central Europe kept the dust airmass and the associated cloudiness trapped until 5 April. In the evening hour an eastward moving Atlantic cold front



finally marked the end of the dust event, as skies cleared up just behind in the replacing clean and subsiding airmass.

In the MSG imagery, cloud cover obscured most of the dust transport towards Europe. The horizontal dust distribution is better seen in the dust AOD maps (Fig. 3) from the COSMO-  
535 MUSCAT simulation at 14 km horizontal resolution. Figure 3a shows an intense dust plume with AOD exceeding 1.5 at the Moroccan/Algerian border on 2 April, 15:00 UTC, which corresponds to the magenta dust signature in the corresponding MSG IR image. Obviously, at this time, Europe was still affected by the remnants of a previous dust outbreak which occurred in late March 2014. In the consecutive image (Fig. 3b), the dust transport to-  
540 wards Europe is clearly depicted within the s-shaped conveyor belt. The initial dust plume is now located over Germany with AOD values still reaching up to 1.5. Furthermore, the model reproduces the significant dust emissions in terms of dust AOD over the desert in Algeria and Tunisia in association with the eastward travelling cold front. In Fig. 3c, the closed circulation centred over Sardinia is clearly seen, with the freshly emitted dust over  
545 Libya being steered increasingly in a cyclonic gyre over the Mediterranean. Meanwhile the dust over central Europe is kept trapped, with the highest dust load found over Austria and southern Germany at AOD values up to 1. On 5 April, 12:00 UTC (Fig. 3d) the dust AOD over Germany is markedly decreased but locally still reaches up to 0.5.

The available AOD observations of AERONET stations (550 nm coarse mode, quality level  
550 2.0) are depicted by colored circles in Fig. 3 for dust model evaluation. On 2 April, 15:00 UTC, observed AOD over Europe is already significantly raised (up to 0.5), which is similar to the model results. On 3 April, 15:00 UTC, observations show a strong zonal gradient in AOD, with strongly elevated values in Tunis and Lindenberg (Germany) (AOD up to 1) and moderately elevated values in northern Germany (AOD up to 0.3), while the  
555 Iberian peninsula was obviously not affected by dust (AOD < 0.01). This is in very good agreement with the simulation. Over the next 2 days, there is a lack of observations over central Europe due to the obscuring cloudiness. However, the AERONET station at Lindenberg shows AOD values up to 0.5 on both 4 and 5 April, 12:00 UTC, which is higher than in the model, where the highest dust loads are displaced more to the south.

560 A statistical evaluation, taking AERONET coarse mode AOD data of level 2.0 quality and corresponding modeled values at the nearest geographical position into account, is shown by the scatter plot in Fig. 4. The considered data set contains 301 observation/model pairs collected over the period 2 April 00:00UTC to 6 April 00:00UTC. Correlation between observational and model data is 0.57. One has to note, however, that the number of observations  
565 directly affected by the dust plume was supposedly lower than usual, due to the extensive cloud cover. The mean AOD of both observations and model data does not differ significantly, as it is  $0.07 \pm 0.06$  and  $0.06 \pm 0.07$  respectively.





Concerning the vertical distribution of mineral dust, Fig. 5a and 5b show dust particle number concentrations  $n_d$  along the meridian  $10^\circ$  E, running through central Germany from the COSMO-MUSCAT simulation at 2.8 km horizontal resolution. The plots confirm that the Sahara dust reached the highest layers of the troposphere, with  $n_d$  locally reaching up to  $1 \times 10^8 \text{ m}^{-3}$ . This is the thousand fold of the climatological mean value of  $1.6 \times 10^5 \text{ m}^{-3}$  as in Phillips et al. (2008). Nearly everywhere in the cross section, the values are above the climatological mean for both 4 and 5 April, 12:00 UTC. Lower values are likely caused by local wet deposition in association with precipitation over northern Germany.

A vertical particle extinction coefficient profile, retrieved from lidar measurements (Baars et al., 2016) at TROPOS in Leipzig provides further valuable information for dust model evaluation (Fig. 6). Albeit averaged for a short time period around 5 April, 21:00 UTC, when the main dust event had already ended over most of Germany, it still shows mineral dust up to an altitude of 7 km. Above this altitude, already clean air had subsided. According to the lidar particle extinction retrievals, the dust was located in two distinct layers. Associated peak values are well above the hundred fold of the corresponding climatological mean value (see blue vertical line). The simulated extinction coefficient profile, which is computed from COSMO-MUSCAT dust concentrations using refractive indices taken from Sinyuk et al. (2003), is in good agreement, as it shows peak values of the same magnitude as well as the strong decline of mineral dust extinction above 6 km altitude. However, the layered structure is not well reproduced. Partly, this can be attributed to black carbon aerosol incorporation, which has very similar absorbing properties as mineral dust, in the lidar observations, which is not considered in the dust simulations by COSMO-MUSCAT. To a large extent, however, this is likely due to a too strong vertical mixing and the potential incorporation of anthropogenic air pollutants within the boundary layer. COSMO-MUSCAT, on the other hand, was only applied to simulate wind-driven dust emissions from soil surfaces.

## 4 Results

### 4.1 Reference model run SMBLK

We first compare the model run SMBLK (see Tab. 1) with single-moment bulk microphysics and without dust feedback on clouds and radiation with the available observational data for an initial assessment of the representation of cloud cover, cloud microphysics and precipitation. For qualitative cloud cover comparison, we derived synthetic infrared satellite images by the application of the infrared forward simulator (see Appendix A) on the model data. Figure 7 shows maps of brightness temperature from MSG SEVIRI and the model run SMBLK over a 24 h period, starting on 4 April, 12:00 UTC. An extensive and optically dense



shield of cirrus clouds traverses the domain in the satellite images. In some areas the associated cloud top temperatures reach below 210K, which corresponds to the tropopause level. Most of this cloudiness is not present in the synthetic images of the model data, where it is mostly limited to the western and northern boundaries. These regions are strongly influenced by the driving boundary fields, as winds mostly prevailed from the west and north. Moreover, cloud top temperatures of cloud fields present in the model are about 20K too warm in comparison with the satellite images. In Fig. 7d and 7f, clouds are completely missing in the southeastern parts of the domain in the model results.

Comparing the available CloudSat data to modeled IWC for the satellite overpass on 4 April around 12:30 UTC in Fig. 8a, reveals a significant lack of IWC above an altitude of 6 km in the model. The discrepancy reaches up to one order of magnitude at 10 km altitude with a modeled value of  $1 \times 10^{-3} \text{ g m}^{-3}$  compared to  $1 \times 10^{-2} \text{ g m}^{-3}$  in the CloudSat retrieval. Moreover, cloud top height in the model is significantly underestimated by about 1 km. However, below 6 km altitude, the modeled along-track averages of IWC are in excellent agreement with observations. The horizontal distribution of mixed phase clouds (not shown) differs considerably, as significant amounts of IWC occur to the north of  $51^\circ \text{ N}$  in the observations, but not in the model. The comparison of the time series of IWC obtained with Cloudnet for the grid cell of the TROPOS site, Leipzig shows quite similar results (Fig. 8b). While IWC steadily increases above an altitude of 7 km and reaches up to  $4 \times 10^{-3} \text{ g m}^{-3}$  at 11 km altitude in the radar profile, the modeled profile shows IWC values fluctuating around  $10^{-4} \text{ g m}^{-3}$  in the same altitude range. However, below 6 km, modeled IWC values are with about  $1 \times 10^{-2} \text{ g m}^{-3}$  significantly higher than the observed values of  $1 \times 10^{-3} \text{ g m}^{-3}$ . In summary, these results confirm the results from the infrared image comparison, as they give a quantitative estimate of the lack of IWC inside cirrus clouds. Cloud infrared absorption and thus simulated cloud top temperatures are strongly dependent on IWC until saturation begins above a value of  $5 \times 10^{-2} \text{ g m}^{-3}$ .

In addition, model precipitation amounts are evaluated, since they also may be affected by the effects of mineral dust. Moreover, we can indirectly infer the distribution of precipitating mixed phase clouds during the evaluation period, which is obscured in the satellite images (Fig. 2). In Fig. 9a, measured 36 h-totals of precipitation (4 April, 00:00 UTC to 5 April, 12:00 UTC) at the various DWD stations in Germany and surrounding areas are compared to the model data. The highest amounts of up to 30 mm rain occurred in northern Germany associated with a nearly stationary warm front. Other than that, isolated precipitation occurred partly triggered by orography, as well as in a curved band over western Germany with totals mostly below 10 mm. While the model agrees well in the maxima of precipitation in association with the warm front, the location of the precipitation band does not match the observations, as it is displaced too far to the northeast over the Baltic



640 Sea (54.5°N, 11.0°E). Even more remarkable is the occurrence of intense precipitation of  
locally more than 30mm in the model linked with convection over western Germany on  
late 4 April, which was not observed at all. As a result, domain-wide precipitation is over-  
estimated in the SMLK run by 64 %.

#### 4.2 Dust sensitivity model runs

645 Having evaluated the model performance of the control run SMLK in the previous Sec-  
tion, this Section is dedicated to the results of the sensitivity study. Again, we begin with  
the comparison of simulated infrared images to corresponding MSG satellite images and  
the estimation of upper tropospheric IWC, which is closely related to infrared tempera-  
tures. To answer the question whether the interactive dust simulation impacts cloud top  
650 temperature in Fig. 10, we compare the run with climatological dust impact (Fig. 10a,c and  
e) to the run IINT with fully interactive dust-cloud and dust-radiation effects (Fig. 10b,d  
and f). The run IINT has more extensive cloud cover due to the impact of the simulated dust  
plume. In the central and southeastern parts of the domain, which are basically cloud-free  
in ICLM but cloud-covered in the MSG images (see Fig. 7), at least fragmented cloudiness  
655 with cloud top temperatures around 220 K is present in IINT. However, the representation  
is still not very realistic, as a coherent cloud shield is still not present (see Fig. 7a,c,e for  
comparison). For a more quantitative estimation of the differences seen in the simulated  
images and the satellite images, a threshold temperature  $T_{tr} = 240$  K is defined, to calculate  
the percentage of pixels colder than  $T_{tr}$  in an hourly image series obtained over the period  
660 from 4 April, 00:00 UTC to 5 April, 12:00 UTC. We are aware that with this approach the dis-  
crimination between cirrus clouds and other cloud types (e.g. convective clouds) cannot  
be assured and furthermore semi-transparent cirrus clouds with brightness temperatures  
 $T_b > 240$  K are not considered. However, given the circumstances of this case study (i.e.  
the predominant occurrence of very cold widespread cirrus clouds in the satellite images),  
665 this should give a reasonably good quantitative estimate of model performance regarding  
cirrus cloud representation. For the respective MSG image series, this value is 76 %, which  
highlights that for most of the time and area, the model domain D2 was covered by cirrus  
clouds. For the run ICLM, this value is 11 %, but increases twofold to 21 % with fully inter-  
active dust effects to in IINT. Nevertheless, this is still only 28 % of the observed value. In  
670 order to trace this sensitivity seen in the infrared images back to cloud microphysics, we  
compare vertical profiles of IWC for the CloudSat overpass and the time series at the TRO-  
POS site. Figure 11 shows the vertical profiles of the model-to-measurement ratio for the  
different runs. The CloudSat comparison reveals an expectedly strong sensitivity to min-  
eral dust, as IWC increases between 200 % and 500 % in the run IINT compared to ICLM.  
675 In the altitude range between 7 km and 11 km, about 10 % of the observed IWC is present



in the run ICLM, but this value increases to about 40 % in the run IINT. The gap to obser-  
vations is however larger in the model near the tropopause at 11.5 km altitude where it is  
in the order of one magnitude (Fig. 11a). At the TROPOS site, a large increase in IWC can  
be seen in the upper troposphere, when considering interactive dust effects in the model  
680 (Fig. 11b). Above 9 km altitude, only about 5 % of observed IWC is present in the run ICLM  
with climatological mean dust effect, but this value increases again to roughly 40 % above  
9 km altitude in the run IINT with fully interactive dust effects. Moreover, in IINT, also the  
representation of precipitation is improved in comparison to the run with single-moment  
bulk microphysics (see Fig. 9b). The geographical distribution of the precipitation band  
685 over northern Germany matches observations better in IINT than in SMLK. The intense  
precipitation band seen in the run SMLK over western Germany is still present in IINT,  
but shows significantly lower totals of up to 20 mm. Generally, precipitation is better repre-  
sented by IINT than SMLK, as domain-wide precipitation is overestimated in by only 6 %  
in IINT but 64 % in SMLK. The correlation coefficient between observational and model  
690 data can be used to estimate the agreement in the geographical distribution of precipita-  
tion. The correlation coefficient is 0.5 in IINT, but only 0.4 in SMLK, suggesting a better  
representation of precipitation in the model run with interactive dust.

To disentangle the different contributing dust-effects to the improved cloud representation,  
we evaluate the additional sensitivity model runs RCLM and CCLM, which have climato-  
695 logical dust-radiation and dust-cloud-activation effects, respectively. Both runs do not dif-  
fer significantly from the run IINT in the infrared simulation, suggesting heterogeneous ice  
nucleation of desert dust being the main contributor to the development of the additional  
cloudiness. This is also reflected in the CloudSat comparison, as even there, the results of  
RCLM and CCLM do not show a clear shift towards higher or lower IWC values compared  
700 to IINT. Only in the comparison at the TROPOS site, there is 80 % less IWC modeled in the  
mixed phase cloud region below 6 km altitude without radiative effects of the dust plume  
in comparison to IINT. Supposedly, dust-radiative effects can affect mixed phase clouds in  
multiple ways and not only by reducing cloud cover through stabilization of the thermal  
stratification of the atmosphere. Dust-radiation effects are also evident in the precipitation  
705 analysis. Comparing the results with fully interactive dust effects (Fig. 9b) to the results  
of climatological dust-radiation effects (Fig. 9c), more widespread precipitation is evident  
over southern Germany in latter case, which is reflected also in a stronger overestimation  
of precipitation by 13 % in RCLM versus 6 % in IINT. This improvement, however, does not  
increase the correlation with observations, with a correlation coefficient of 0.5 for IINT and  
710 RCLM respectively.

The last sensitivity model run IAIP is used to evaluate the alternative INP-parameterization  
P08 in comparison with the parameterization U17. This is to assess a range of uncertainty



due to uncertainties in the freezing properties of mineral dust. In the infrared satellite im-  
ages, IAIP produces the lowest cirrus cloud cover with only 7%, which is 3 times lower  
715 compared than in IINT. Similarly, in the CloudSat comparison in Fig. 11, IAIP shows the  
lowest IWC values, except near the tropopause, where the run SMLBK shows the lowest  
values. Above 6 km altitude, the difference between IAIP and IINT is particularly large  
with mostly only 10 % IWC present in IAIP. Even more drastic differences are seen in the  
comparison at TROPOS at 9 km altitude, where only 0.1 % of the observed IWC are present  
720 in the IAIP run. For the tested INP-parameterizations, INAS-density as the measure of  
activity differs by the order of several magnitudes in the deposition freezing range (not  
shown here). These uncertainties obviously affect the model performance to a similar  
extent than the uncertainties in the representation of mineral dust concentrations in the  
model.  
725 Table 3 summarizes the most important findings of the sensitivity studies presented in this  
Section.

**Table 3.** Summary table of the sensitivity study: the cirrus cloud fraction estimation is based on  
the infrared temperature simulation. IWC in cirrus clouds is the calculated mean IWC inside the  
layer above 9 km altitude for both comparisons (CloudSat and TROPOS). Precipitation deviation is  
calculated as the relative deviation of the sum of modeled 36 h-totals at all stations from the sum of  
corresponding measurements.

Data	Cirrus		Precipitation	
	cloud cover [%]	IWC [ $\text{g m}^{-3}$ ]	overestimation	correlation
<b>Observation</b>	76	$5 \times 10^{-3}$	-	-
<b>SMLBK</b>	-	$9 \times 10^{-4}$	59	0.38
<b>ICLM</b>	11	$7 \times 10^{-4}$	21	0.50
<b>IINT</b>	21	$2 \times 10^{-3}$	6	0.50
<b>RCLM</b>	22	$2 \times 10^{-3}$	13	0.53
<b>CCLM</b>	21	$2 \times 10^{-3}$	8	0.49
<b>IAIP</b>	7	$3 \times 10^{-4}$	-4	0.34

### 4.3 Detailed evaluation of cloud microphysics

In this section, detailed cloud-microphysics data of the ML-CIRRUS flights conducted on  
3 April and 4 April, respectively, are analyzed. A description of the data sets used and the  
730 methodology for data processing are presented in Sect. 2.3.4. In a second part, the ML-  
CIRRUS data from 3 April is compared to model results, and the sensitivity of modeled ice



particle diameter  $D_i$  to heterogeneous ice nucleation of mineral dust is evaluated.

Observed IWC along trajectories of both flights on 3 April and 4 April is shown in Fig. 12 underlaid with MSG infrared of cloud cover. Accordingly, on 3 April, HALO did not  
735 sample the main cloud shield but broken cirrus clouds at 8 to 12 km altitude. In addition, a stratiform cloud shield below 7 km altitude was probed during ascent and descent at start and landing. IWC within cirrus clouds reached up to  $10^{-2} \text{ g m}^{-3}$  during this flight (Fig. 12a). On 4 April, HALO headed westward to Portugal and passed at an altitude of 9.5 km through a dense band of cirrus clouds located to the north of the Alps (Fig. 12b). Cloud  
740 top temperatures of this cirrus were much lower than those of cirrus clouds sampled on 3 April. IWC measured within the clouds on 4 April is partly above  $10^{-1} \text{ g m}^{-3}$ , which is more than one order of magnitude higher than on 3 April.

Figure 13 shows ice particle number densities [ $\text{m}^{-3} \mu\text{m}^{-1}$ ] as colored shadings for both flights averaged along the flight trajectory. Accordingly, on 3 April, the highest particle  
745 densities can be found in the smallest size bins with particle diameters lower than  $67.5 \mu\text{m}$  (Fig. 13a). Especially high particle number densities of up to  $5 \times 10^3 \text{ m}^{-3} \mu\text{m}^{-1}$  occur at the cloud tops, indicating the influence of aviation induced contrail cirrus. The decline in particle number density with increasing diameter is monotonic, with the largest particles having a diameter of around  $200 \mu\text{m}$ . The number-averaged mean diameter  $\bar{D}_N$  depicted  
750 by the solid line and the top axis in Fig. 13 increases nearly linearly from  $25 \mu\text{m}$  at 11 km altitude to  $55 \mu\text{m}$  at 9 km altitude. This suggests diffusional growth of settling ice particles before they begin to sublimate below 9 km altitude near the cloud base. According to measured prevalent particle sizes, cirrus clouds sampled on 3 April can be classified as in situ origin cirrus (Luebke et al., 2016). For the cloud sampled on 4 April, the main distinguish-  
755 ing characteristics of the clouds sampled on 3 April are the much broader PSD along with much higher particle number densities. This is especially pronounced near  $20 \mu\text{m}$  with values up to  $10^5 \text{ m}^{-3} \mu\text{m}^{-1}$ , which is close to 100 fold the value measured on 3 April. The PSD again shows a monotonic decrease of particle densities with increased particle sizes, with no hints of a bi-modular structure.  $\bar{D}_N$  is between  $35 \mu\text{m}$  and  $40 \mu\text{m}$  in the height range of  
760 8 to 9.5 km, which is slightly lower than  $\bar{D}_N$  on 3 April.

On basis of these observations, the optically dense cirrus cloud sampled on 4 April can also be classified as in situ origin cirrus, as small particles are obviously dominating. Furthermore it is likely, that the additionally available humidity to be converted into IWC on 4 April was not consumed by larger ice crystals but new ice particles. This points toward  
765 a higher INP concentration on 4 April than on 3 April, which is supported by NIXE-CAS aerosol measurements in the diameter range of  $0.6 - 2 \mu\text{m}$ .

Moreover, simulated dust-particle number concentrations  $n_d$  inside sampled clouds for both flights differed significantly (not shown), as on 3 April  $n_d$  ranged from  $3 \times 10^4 \text{ m}^{-3}$



to  $2 \times 10^6 \text{ m}^{-3}$  but on 4 April  $n_d$  was consistently above  $4 \times 10^6 \text{ m}^{-3}$  and reached even up  
770 to above  $10^7 \text{ m}^{-3}$  for a small part of the flight track. This underpins the assumption of the  
higher INP-concentrations affecting clouds on 4 April.

To assess whether the model shows a similar behaviour with enhanced heterogeneous ice  
nucleation, scatter plots of modeled  $D_i$  for the three sensitivity model runs ICLM, IINT  
and IAIP are plotted in Fig. 14 against the ML-CIRRUS data for 3 April. Furthermore,  
775 values of  $\bar{D}_N$ , as well as  $\bar{D}_{IWC}$  are calculated for all data sets (see Eq. 13 and 14). In the  
run ICLM, which considers the climatological dust concentration, data points are shifted to  
too high values of modeled vs. measured  $D_i$  for high IWC values larger than  $10^{-3} \text{ g m}^{-3}$ ,  
while the contrary is the case for the IWC values lower than  $10^{-3} \text{ g m}^{-3}$  (Fig. 14 a). This  
asymmetry results in  $\bar{D}_N = 27 \mu\text{m}$  for the model, which is smaller than the measured value  
780 of  $38 \mu\text{m}$ . The contrary is the case for the IWC-weighted average, which puts more weight  
on the larger ice particles, with  $\bar{D}_{IWC} = 72 \mu\text{m}$  in the model and  $\bar{D}_{IWC} = 53 \mu\text{m}$  in the mea-  
surements. This suggests, that at low values of IWC, INPs activate very efficiently in the  
model with the parameterization U17. However, at larger IWC values, supposedly there  
are not enough INPs available (constrained by the climatological mean dust concentration)  
785 in ICLM for the formation of additional ice crystals. With interactive dust in IINT, we ob-  
serve a large decrease in  $D_i$  in the denser cloud parts with high IWC (Fig. 14 b). For most  
of the data points, simulated  $n_d$  is above the climatological mean, thus making additional  
INPs available for ice nucleation in the parts of clouds, while ice nucleation is limited in  
ICLM. This is reflected in a 46% decrease of  $\bar{D}_{IWC}$  to  $39 \mu\text{m}$ , while  $\bar{D}_N$  decreases by only  
790 8% to  $25 \mu\text{m}$  compared to ICLM. With the application of the parameterization P08 in the  
run IAIP, for the whole IWC spectrum, modeled  $D_i$  is larger than for the measurements,  
suggesting the presence of abundant potential INPs, which, however, do not activate effi-  
ciently (Fig. 14 c).

Figures 14d to 14f show simulated infrared images for the runs ICLM, IINT, and IAIP, re-  
795 spectively. From the sensitivity of cold cloud cover to ice nucleation we can conclude that  
the decrease in  $D_i$  in dense cloud regions in response to raised INP-concentrations (positive  
Twomey effect) is the main reason for the additional cirrus cloud formation in the model,  
as it occurs significantly only in the run IINT. A larger number of ice crystals increases the  
cloud optical depth (COD), which our model can account for, as the cloud-radiation scheme  
800 uses prognostic effective diameters  $D_i^{ef}$  from the two-moment microphysics scheme (see  
Sect. 2.1.4). This increase in COD increases long-wave emissions at the cloud tops, further  
cooling these regions and enhancing updraughts inside cirro-cumulus clouds. This even-  
tually causes cloud cover to increase in our model. However, cloudy parts which are less  
dense are not susceptible to this feedback mechanism, as otherwise we would observe an  
805 increase in cloud cover using U17 independently of the representation of mineral dust in





the model. Thus, higher than climatological mean mineral dust concentrations in the model are necessary for additional cirrus cloud formation in this study. Our reasoning is further underpinned by the fact, that without detailed cloud-radiation interactions, no significant sensitivity to mineral dust can be observed in our model runs.

810 In order to assess the limitations in cirrus cloud representation in the simulations due to an inaccurate representation of the thermodynamic environment, we further evaluate vertical profiles of specific humidity (SH) obtained from radiosoundings over Germany (see Sect. 2.3.5). Figure 15a shows radiosonde profiles for the dates 4 April, 00:00 UTC, 4 April, 12:00 UTC and 5 April, 00:00 UTC, respectively. There is a tendency of water vapor to increase over the considered time period in a layer at approximately 7 km altitude, which is most pronounced between 4 April, 00:00 UTC and 4 April, 12:00 UTC, when the dense cirrus canopy appears in the simulation domain. Figure 15b shows modeled to measured ratios of SH for the IINT run. On 4 April, 00:00 UTC, the model has 40 % higher values of SH below 8 km than measured. Above 11 km altitude, the modeled SH is significantly  
820 higher than in the observed, but this seems more likely caused by the inaccurate representation of tropopause height in the model. On 4 April, 12:00 UTC, there is less SH present in the model in an altitude range between 7 km and 11 km. This becomes even more evident on 5 April, 00:00 UTC, when only 60 % of measured SH is present in the model. Thus, the model does not seem to follow the trend of increasing SH over time as seen in the  
825 radiosonde profiles. There can be different reasons for these observations. Obviously, there is a large vertical gradient in SH, and turbulent transport associated with cloud development could easily modify the vertical distribution of SH. However, the layer with the relatively dry air is located at the cirrus cloud base or below. So turbulent mixing associated with cirrus formation should not affect this layer at all, and in fact, no significant differences are  
830 found between the model runs. More likely this is caused by an inaccurate representation of humidity in the meteorological boundary data. Supposedly, the thermodynamic environment inside dust plumes is affected by the dust in manifold ways during the long-range transport from the Sahara to Europe, which was not represented in the boundary data.

## 835 5 Summary and Conclusions

The aim of this study was to model the impact of desert dust on cloud development for the dust outbreak in early April 2014. Therefore we used the regional dust model COSMO-MUSCAT to simulate dust emission and dust transport from northern Africa toward Europe, as well as dust-radiation and dust-cloud interactions over Germany. For reference,  
840 a first model run with COSMO using the operational single-moment bulk microphysics



scheme and without dust-radiation and dust-cloud interactions was performed for Germany on a grid with 2.8 km horizontal spacing over the period 3 April, 12:00 UTC to 5 April, 12:00 UTC. Simulated cloud top temperatures of this model run were compared to MSG infrared imagery, and modeled IWC to cloud radar retrievals from CloudSat satellite  
845 and measured at TROPOS site in Leipzig. We qualitatively found a large deficit in modeled cirrus cloud cover over the 48 h period, which coincided with above-average mineral dust concentrations throughout the height range of the troposphere. The lack in cirrus clouds was also seen in the comparison of IWC, as only 10% of observed IWC was present in the model at the relevant altitudes. Moreover, modeled precipitation were overestimated  
850 by 64% on average if compared to DWD station records. Thus, these results showed a strong misrepresentation of cloudiness and precipitation, possibly linked to the neglect of interactive dust effects in the model during the Saharan dust event. By interactive dust modeling with a two-moment microphysics scheme (Seifert and Beheng, 2006) including dust-radiation, dust-cloud activation and detailed dust-ice nucleation effects, the question  
855 is investigated whether with this more detailed approach cloud and precipitation representation can be improved in the model. Based on the Saharan dust distribution modeled with COSMO-MUSCAT on a domain with 14 km grid spacing and covering northern Africa and Europe, 5 sensitivity model runs were performed with COSMO-MUSCAT with 2.8 km horizontal resolution over Germany. The setup of these runs included a run with fully interactive dust effects, a run with a spatially and temporally uniform climatological low average  
860 dust concentration prescribed in the radiation and cloud schemes and two runs with climatological dust-radiation effects and dust-cloud activation effects, respectively. While for these model runs the ice parameterization of Ullrich et al. (2017) (U17) was used, an additional fully interactive model run using the parameterization of Phillips et al. (2008) (P08)  
865 was performed to assess the uncertainty related to the choice of the ice parameterization. The evaluation of the modeled dust fields with AERONET data and an aerosol extinction profile retrieved from lidar data at the TROPOS site in Leipzig showed a reasonably good agreement with observations. Uncertainties can be related to the presence of other aerosol components (e.g. black carbon and organic aerosol), which were not simulated  
870 with COSMO-MUSCAT.

Comparing the two model runs either using fully interactive or fully prescribed from climatology dust interactions, we found a strong sensitivity of cloud formation to mineral dust concentrations. Cirrus cloud cover doubled and IWC increased by a factor of 2 to 8 inside the cirrus layer, reaching up to about 40% of the observed values from CloudSat  
875 satellite and TROPOS site cloud radar, due to the feedback of the online-simulated dust concentrations.

This sensitivity was found primarily due to increased heterogeneous ice nucleation of min-



880 eral dust, as the two additional sensitivity model runs using climatological mean mineral dust concentrations either for radiation interaction or cloud activation respectively, produced the same results for cirrus clouds as with the fully interactive run. Radiative effects of the dust plume predominantly had an impact on precipitation formation in southern Germany. Dust-cloud-activation effects were not discernible, which suggests that in our study the assumed aerosol background dominated this process even in the presence of the simulated mineral dust concentrations.

885 Lastly, the choice of the INP-parameterization turned out to be at least as important as the application of a more realistic spatially and temporally varying mineral dust distribution, and the parameterization of Ullrich et al. (2017) led to the best agreement of model results with observations.

Evaluating ice cloud microphysics in more detail with in situ measurements obtained during the ML-CIRRUS aircraft campaign showed that in general the two-moment microphysics scheme of Seifert and Beheng (2006) along with the modifications done to include detailed dust-cloud interactions was capable of reproducing realistic particle diameters inside cirrus clouds. Homogeneous ice nucleation of liquid aerosol particles was not important in our model, as supersaturation over ice was consistently below the homogeneous freezing threshold given in Kärcher and Lohmann (2002). Thus, heterogeneous ice nucleation controlled particle concentrations and diameters inside in situ formed cirrus clouds. In fact, we could see a strong sensitivity of modeled ice particle sizes to mineral dust concentrations, and the smallest particle diameters with best agreement to measurements were found using interactive dust simulation with the U17 parameterization. The occurrence of the positive Twomey effect in response to high mineral dust concentrations fostered the development of more extensive cirrus clouds in our model due to dust-cloud-radiation effects represented in the radiation scheme extended by Dipu et al. (2017).

The improvements seen in our model still cannot be considered adequate for a realistic representation of cirrus cloud cover. This limitation was likely inflicted by the meteorological boundary fields, which underestimated humidity in layers relevant for cirrus cloud formation. In this regard, it would be useful to raise specific humidity inside selected vertical layers in the boundary data to match observed values in order to test the cloud representation and sensitivity to mineral dust in additional model runs with adjusted input data. However, this was beyond the scope of this paper.

910 Based on the outcomes of the present sensitivity study, we recommend to test this or similar modeling approaches for other individual cases, which are characterized by extensive cirrus cloud development in association with major desert dust outbreaks into the mid-latitudes. It has to be shown, on a statistical basis, whether weather forecast quality during such periods can indeed take advantage of the more detailed but also numerically more



915 expensive interactive weather-dust simulations. For future research, more field studies  
investigating microphysical properties of cirrus clouds affected by mineral dust could pro-  
vide valuable information for model evaluation to corroborate our findings. Multi-spectral  
satellite observations and derived cloud products can further improve the ability to char-  
acterize the spatial distribution of cirrus clouds with lower optical thicknesses to compare  
920 their representation in simulations. In addition, further aircraft in situ ice nucleation exper-  
iments are needed to reduce the remaining uncertainties in parameterized INP properties  
of mineral dust and aerosol in general.

### Acknowledgments

The authors thank the Deutscher Wetterdienst (DWD) for good cooperation and support.  
925 We are grateful for computing time from the German Climate Computing Center (DKRZ).  
The research leading to these results has partly received funding from ACTRIS-2 in HORI-  
ZON 2020 under grant agreement no. 654109. CV thanks for funding by the DFG within the  
SPP1294 HALO under contract no VO 1504/4-1 and by the Helmholtz Association under  
contract no W2/W3-60. We thank the PI investigators and their staff for establishing and  
930 maintaining the AERONET sites used in this investigation. EUMETSAT is acknowledged  
for providing MSG SEVIRI data. CloudSat data has been provided by the NASA Langley  
Research Center Atmospheric Science Data Center, and Atmospheric Sounding profiles by  
the University of Wyoming.

### Appendix A

#### 935 Infrared satellite imagery simulation

To take advantage of prognostic cloud particle number concentrations in the runs using  
two-moment microphysics for synthetic infrared image derivation, an appropriate radia-  
tive transfer model was constructed in the framework of this study. It is based on ab-  
sorption and emission of black body radiation at thermodynamic equilibrium and neglects  
940 scattering of thermal radiation. The absorption coefficient is calculated as the linear com-  
bination of the individual absorption by the modeled six hydrometeor classes, as well as  
absorption by water vapour. For cloud ice and cloud water, additionally, parameterized  
sub-grid scale mass contents are considered. The selected PSD for all classes is a gener-  
alized gamma function, in accordance with the two-moment microphysics scheme, and  
945 parameters are adopted from the currently used version in this study.  
For the spherical particle classes graupel, rain and hail, which contain exclusively particles  
larger by orders of magnitude than the considered wavelength, a constant absorption ef-



950 efficiency of 0.95 is assumed for calculating absorption coefficients based on the geometric cross section. Cloud ice and snow are treated in common, and are assumed to consist of hexagonal plates. For this particle class, the absorption coefficient is parameterized using polynomial approximations to exact Mie-calculations (Fu et al., 1998). Therefore,  $D_i^{ef}$  is inferred from  $D_i$  by taking the size-dependent linear dimension relationships for hexagonal plates given in Fu et al. (1998). Cloud droplets are treated as spherical particles and the absorption parameterization of Lindner and Li (2000) is used. To account for water vapor absorption an empirical formulation based on the water vapor mixing ratio being valid for a reference pressure and temperature is scaled to the actual pressure and temperature value (Chou and Suarez, 1994). The emitted radiation of the Earth's surface is approximated with a surface emissivity ranging from 0.95 for surface temperatures lower than 273 K to 0.85 for surface temperatures above 280 K. To account for the effects of a slanted satellite viewing angle, the derived optical thicknesses are inversely scaled with the cosine of the satellite viewing angle, calculated for the satellite position  $0^\circ\text{N}$ ,  $0^\circ\text{E}$  and the geographical position of the referred model grid point.

To make the infrared simulation also applicable to model data with single-moment microphysics, particle diameters either have to be assumed or parameterized of other prognostic quantities. Here, we assume a constant diameter of  $D_c = 10\ \mu\text{m}$  for cloud droplets and  $D_r = 10^3\ \mu\text{m}$  for rain droplets.  $D_i$  is parameterized with IWC, containing the contributions of modeled  $q_i$  and  $q_s$ . A parameterization was constructed, using ML-CIRRUS data for 3 and 4 April respectively, and is given by the following analytical expression:

$$D_i = [0.044531 \times \log_{10}(\text{IWC}) + 1.554498]^{0.1}, \quad (\text{A1})$$

970 where IWC is given in units of  $[\text{g m}^{-3}]$  and  $D_i$  in  $[\mu\text{m}]$ . This expression gives reasonable  $D_i$  ranging from  $8\ \mu\text{m}$  for  $\text{IWC} = 10^{-7}\ \text{g m}^{-3}$  to  $65\ \mu\text{m}$  for  $\text{IWC} = 10^{-1}\ \text{g m}^{-3}$ .

For the single-moment bulk microphysics run, and using this parameterization, we compared simulated brightness temperatures with the more comprehensive (treatment of scattering) Radiative Transfer model for TIROS Operational Vertical sounder (RTTOV) model (Saunders et al., 2018), and found a very good agreement with our radiative transfer scheme, as simulated temperatures differed by not more than 5 K, which is in the order of typical uncertainties (Senf and Deneke, 2017).



## References

- 980 AbdulRazzak, H. and Ghan, S. J.: A parameterization of aerosol activation: 2. Multiple aerosol types, *Journal of Geophysical Research: Atmospheres*, 105, 6837–6844, doi:10.1029/1999JD901161, 2000.
- Austin, R. T., Heymsfield, A. J., and Stephens, G. L.: Retrieval of ice cloud microphysical parameters using the CloudSat millimeter-wave radar and temperature, *Journal of Geophysical Research: Atmospheres*, 114, doi:10.1029/2008JD010049, 2009.
- 985 Baars, H., Kanitz, T., Engelmann, R., Althausen, D., Heese, B., Komppula, M., Preißler, J., Tesche, M., Ansmann, A., Wandinger, U., Lim, J.-H., Ahn, J. Y., Stachlewska, I. S., Amiridis, V., Marinou, E., Seifert, P., Hofer, J., Skupin, A., Schneider, F., Bohlmann, S., Foth, A., Bley, S., Pfüller, A., Giannakaki, E., Lihavainen, H., Viisanen, Y., Hooda, R. K., Pereira, S. N., Bortoli, D., Wagner, F., Mattis, I., Janicka, L., Markowicz, K. M., Achtert, P., Artaxo, P., Pauliquevis, T., Souza, R. A. F.,
- 990 Sharma, V. P., van Zyl, P. G., Beukes, J. P., Sun, J., Rohwer, E. G., Deng, R., Mamouri, R.-E., and Zamorano, F.: An overview of the first decade of Polly<sup>NET</sup>: an emerging network of automated Raman-polarization lidars for continuous aerosol profiling, *Atmospheric Chemistry and Physics*, 16, 5111–5137, doi:10.5194/acp-16-5111-2016, 2016.
- Bangert, M., Kottmeier, C., Vogel, B., and Vogel, H.: Regional scale effects of the aerosol cloud interaction simulated with an online coupled comprehensive chemistry model, *Atmospheric Chemistry and Physics*, 11, 4411–4423, doi:10.5194/acp-11-4411-2011, 2011.
- Bangert, M., Nenes, A., Vogel, B., Vogel, H., Barahona, D., Karydis, V. A., Kumar, P., Kottmeier, C., and Blahak, U.: Saharan dust event impacts on cloud formation and radiation over Western Europe, *Atmospheric Chemistry and Physics*, 12, 4045–4063, doi:10.5194/acp-12-4045-2012, 2012.
- 1000 Barahona, D. and Nenes, A.: Parameterizing the competition between homogeneous and heterogeneous freezing in cirrus cloud formation - monodisperse ice nuclei, *Atmospheric Chemistry and Physics*, 9, 369–381, doi:10.5194/acp-9-369-2009, 2009.
- Barkan, J., Alpert, P., Kutiel, H., and Kishcha, P.: Synoptics of dust transportation days from Africa toward Italy and central Europe, *Journal of Geophysical Research: Atmospheres*, 110, doi:10.1029/2004JD005222, 2005.
- 1005 Baumgardner, D., Jonsson, H., Dawson, W., O'Connor, D., and Newton, R.: The cloud, aerosol and precipitation spectrometer: a new instrument for cloud investigations, *Atmospheric Research*, 59–60, 251–264, doi:10.1016/S0169-8095(01)00119-3, 2001.
- Berge, E.: Coupling of wet scavenging of sulphur to clouds in a numerical weather prediction model, *Tellus B*, 45, 1–22, doi:10.1034/j.1600-0889.1993.00001.x, 1993.
- 1010 Boose, Y., Sierau, B., García, M. I., Rodríguez, S., Alastuey, A., Linke, C., Schnaiter, M., Kupiszewski, P., Kanji, Z. A., and Lohmann, U.: Ice nucleating particles in the Saharan Air Layer, *Atmospheric Chemistry and Physics*, pp. 9067–9087, doi:10.5194/acp-16-9067-2016, 2016.
- Bégué, N., Tulet, P., Pelon, J., Aouizerats, B., Berger, A., and Schwarzenboeck, A.: Aerosol processing and CCN formation of an intense Saharan dust plume during the EUCAARI 2008 campaign, *Atmospheric Chemistry and Physics*, 15, 3497–3516, doi:10.5194/acp-15-3497-2015, 2015.
- Bühl, J., Seifert, P., Wandinger, U., Baars, H., Kanitz, T., Schmidt, J., Myagkov, A., Engelmann, R., Skupin, A., Heese, B., Klepel, A., Althausen, D., and Ansmann, A.: LACROS: the Leipzig Aerosol



- and Cloud Remote Observations System, Proc.SPIE, 8890, 8890 – 8890 – 6, doi:10.1117/12.2030911,  
1020 2013.
- Carslaw, K. S., Boucher, O., Spracklen, D. V., Mann, G. W., Rae, J. G. L., Woodward, S., and Kulmala,  
M.: A review of natural aerosol interactions and feedbacks within the Earth system, Atmospheric  
Chemistry and Physics, 10, 1701–1737, doi:10.5194/acp-10-1701-2010, 2010.
- Chaboureau, J., Richard, E., Pinty, J., Flamant, C., Girolamo, P. D., Kiemle, C., Behrendt, A., Chep-  
fer, H., Chiriaco, M., and Wulfmeyer, V.: Long range transport of Saharan dust and its radiative  
1025 impact on precipitation forecast: a case study during the Convective and Orographically induced  
Precipitation Study (COPS), Quarterly Journal of the Royal Meteorological Society, 137, 236–251,  
doi:10.1002/qj.719, 2011.
- Chou, M.-D. M. and Suarez, M. J.: An Efficient Thermal Infrared Radiation Parameterization For Use  
1030 In General Circulation Models, 1994.
- Cotton, R. J. and Field, P. R.: Ice nucleation characteristics of an isolated wave cloud, Quarterly Jour-  
nal of the Royal Meteorological Society, 128, 2417–2437, doi:10.1256/qj.01.150, 2002.
- DeMott, P. J., Sassen, K., Poellot, M. R., Baumgardner, D., Rogers, D. C., Brooks, S. D., Prenni, A. J.,  
and Kreidenweis, S. M.: African dust aerosols as atmospheric ice nuclei, Geophysical Research  
1035 Letters, 30, 1732, doi:10.1029/2003GL017410, 2003.
- DeMott, P. J., Prenni, A. J., Liu, X., Kreidenweis, S. M., Petters, M. D., Twohy, C. H., Richardson, M. S.,  
Eidhammer, T., and Rogers, D. C.: Predicting global atmospheric ice nuclei distributions and their  
impacts on climate, 107, 11 217–11 222, doi:10.1073/pnas.0910818107, 2010.
- DeMott, P. J., Prenni, A. J., McMeeking, G. R., Sullivan, R. C., Petters, M. D., Tobo, Y., Niemand, M.,  
1040 Möhler, O., Snider, J. R., Wang, Z., and Kreidenweis, S. M.: Integrating laboratory and field data  
to quantify the immersion freezing ice nucleation activity of mineral dust particles, Atmospheric  
Chemistry and Physics, 15, 393–409, doi:10.5194/acp-15-393-2015, 2015.
- Dipu, S., Quaas, J., Wolke, R., Stoll, J., Mühlbauer, A., Sourdeval, O., Salzmänn, M., Heinold, B., and  
Tegen, I.: Implementation of aerosol–cloud interactions in the regional atmosphere–aerosol model  
1045 COSMO-MUSCAT(5.0) and evaluation using satellite data, Geoscientific Model Development, 10,  
2231–2246, doi:10.5194/gmd-10-2231-2017, 2017.
- Doms, G.: A Revised Cloud Microphysical Parameterization for COSMO-LME, COSMO Newsletter,  
7, 25-28 (available from [www.cosmo-model.org/content/model/documentation/newsLetters/  
newsLetter07](http://www.cosmo-model.org/content/model/documentation/newsLetters/newsLetter07)), 2008.
- 1050 Doms, G. and Baldauf, M.: A Description of the Nonhydrostatic Regional COSMO-Model Part I:  
Dynamics and Numerics, 2015.
- Doms, G., Förstner, J., Heise, E., Herzog, H.-J., Mironov, D., Raschendorfer, M., Reinhardt, T., Ritter,  
B., Schrodin, R., Schulz, J.-P., and Vogel, G.: A Description of the Nonhydrostatic Regional COSMO  
Model Part II: Physical Parameterization, 2011.
- 1055 ECMWF: Part IV: Physical Processes in IFS Documentation CY43R3, 2017.
- Engelmann, R., Kanitz, T., Baars, H., Heese, B., Althausen, D., Skupin, A., Wandinger, U., Komppula,  
M., Stachlewska, I. S., Amiridis, V., Marinou, E., Mattis, I., Linné, H., and Ansmann, A.: The auto-  
mated multiwavelength Raman polarization and water-vapor lidar Polly<sup>XT</sup>: the neXT generation,





- Atmospheric Measurement Techniques, 9, 1767–1784, doi:10.5194/amt-9-1767-2016, 2016.
- 1060 Fridlind, A. M., Ackerman, A. S., Jensen, E. J., Heymsfield, A. J., Poellot, M. R., Stevens, D. E., Wang, D., Miloshevich, L. M., Baumgardner, D., Lawson, R. P., Wilson, J. C., Flagan, R. C., Seinfeld, J. H., Jonsson, H. H., VanReken, T. M., Varutbangkul, V., and Rissman, T. A.: Evidence for the Predominance of Mid-Tropospheric Aerosols as Subtropical Anvil Cloud Nuclei, 304, 718–722, doi:10.1126/science.1094947, 2004.
- 1065 Fu, Q., Yang, P., and Sun, W. B.: An Accurate Parameterization of the Infrared Radiative Properties of Cirrus Clouds for Climate Models, *Journal of Climate*, 11, 2223–2237, doi:10.1175/1520-0442(1998)011(2223:AAPOTI)2.0.CO;2, 1998.
- Gillani, N. V., Schwartz, S. E., Leaitch, W. R., Strapp, J. W., and Isaac, G. A.: Field observations in continental stratiform clouds: Partitioning of cloud particles between droplets and unactivated interstitial aerosols, *Journal of Geophysical Research: Atmospheres*, 100, 18 687–18 706, doi:10.1029/95JD01170, 1995.
- 1070 Görzdorf, U., Lehmann, V., Bauer-Pfundstein, M., Peters, G., Vavriv, D., Vinogradov, V., and Volkov, V.: A 35-GHz Polarimetric Doppler Radar for Long-Term Observations of Cloud Parameters—Description of System and Data Processing, *Journal of Atmospheric and Oceanic Technology*, 32, 675–690, doi:10.1175/JTECH-D-14-00066.1, 2015.
- 1075 Hallberg, A., Noone, K., Ogren, J., Svenningsson, I., Flossmann, A., Wiedensohler, A., Hansson, H., Heintzenberg, J., Anderson, T. L., Arends, B., and Maser, R.: Phase partitioning of aerosol particles in clouds at Kleiner Feldberg, *Journal of Atmospheric Chemistry*, 19, 107–127, doi:10.1007/BF00696585, 1994.
- 1080 Hande, L. B., Engler, C., Hoose, C., and Tegen, I.: Seasonal variability of Saharan desert dust and ice nucleating particles over Europe, *Atmospheric Chemistry and Physics*, 15, 4389–4397, doi:10.5194/acp-15-4389-2015, 2015.
- Heinold, B., Helmert, J., Hellmuth, O., Wolke, R., Ansmann, A., Marticorena, B., Laurent, B., and Tegen, I.: Regional modeling of Saharan dust events using LM-MUSCAT: Model description and case studies, *Journal of Geophysical Research: Atmospheres*, 112, 204, doi:10.1029/2006JD007443, 2007.
- 1085 Heinold, B., Tegen, I., Schepanski, K., Tesche, M., Esselborn, M., Freudenthaler, V., Gross, S., Kandler, K., Knipperitz, P., Müller, D., Schladitz, A., Toledano, C., Weinzierl, B., Ansmann, A., Althausen, D., Müller, T., Petzold, A., and Wiedensohler, A.: Regional modelling of Saharan dust and biomass burning smoke, *Tellus B*, 63, 781–799, doi:10.1111/j.1600-0889.2011.00570.x, 2011.
- 1090 Helmert, J., Heinold, B., Tegen, I., Hellmuth, O., and Wendisch, M.: On the direct and semidirect effects of Saharan dust over Europe: A modeling study, *Journal of Geophysical Research: Atmospheres*, 112, 208, doi:10.1029/2006JD007444, 2007.
- Hiranuma, N., Paukert, M., Steinke, I., Zhang, K., Kulkarni, G., Hoose, C., Schnaiter, M., Saathoff, H., and Möhler, O.: A comprehensive parameterization of heterogeneous ice nucleation of dust surrogate: laboratory study with hematite particles and its application to atmospheric models, *Atmospheric Chemistry and Physics*, 14, 13 145–13 158, doi:10.5194/acp-14-13145-2014, 2014.
- Hobbs, P. V. and Rangno, A. L.: Ice Particle Concentrations in Clouds, *Journal of the Atmospheric*



- Sciences, 42, 2523–2549, doi:10.1175/1520-0469(1985)042<2523:IPCIC>2.0.CO;2, 1985.
- 1100 Hogan, R. J., Mittermaier, M. P., and Illingworth, A. J.: The Retrieval of Ice Water Content from Radar Reflectivity Factor and Temperature and Its Use in Evaluating a Mesoscale Model, *Journal of Applied Meteorology and Climatology*, 45, 301–317, doi:10.1175/JAM2340.1, 2006.
- Holben, B., Eck, T., Slutsker, I., Tanré, D., Buis, J., Setzer, A., Vermote, E., Reagan, J., Kaufman, Y., Nakajima, T., Lavenu, F., Jankowiak, I., and Smirnov, A.: AERONET—A Federated Instrument
- 1105 Network and Data Archive for Aerosol Characterization, *Remote Sensing of Environment*, 66, 1 – 16, doi:10.1016/S0034-4257(98)00031-5, 1998.
- Huneeus, N., Schulz, M., Balkanski, Y., Griesfeller, J., Prospero, J., Kinne, S., Bauer, S., Boucher, O., Chin, M., Dentener, F., Diehl, T., Easter, R., Fillmore, D., Ghan, S., Ginoux, P., Grini, A., Horowitz, L., Koch, D., Krol, M. C., Landing, W., Liu, X., Mahowald, N., Miller, R., Morcrette,
- 1110 J.-J., Myhre, G., Penner, J., Perlwitz, J., Stier, P., Takemura, T., and Zender, C. S.: Global dust model intercomparison in AeroCom phase I, *Atmospheric Chemistry and Physics*, 11, 7781–7816, doi:10.5194/acp-11-7781-2011, 2011.
- Illingworth, A. J., Hogan, R. J., O'Connor, E., Bouniol, D., Brooks, M. E., Delanoé, J., Donovan, D. P., Eastment, J. D., Gaussiat, N., Goddard, J. W. F., Haefelin, M., Baltink, H. K., Krasnov, O. A., Pelon,
- 1115 J., Piriou, J.-M., Protat, A., Russchenberg, H. W. J., Seifert, A., Tompkins, A. M., van Zadelhoff, G.-J., Vinit, F., Willén, U., Wilson, D. R., and Wrench, C. L.: Cloudnet, *Bulletin of the American Meteorological Society*, 88, 883–898, doi:10.1175/BAMS-88-6-883, 2007.
- Jacobson, M. Z.: Development and application of a new air pollution modeling system - Part III. Aerosol-phase simulations, *Atmospheric Environment*, 31, 587 – 608, doi:10.1016/S1352-2310(96)
- 1120 00201-4, 1997.
- Jonson, J., Bartnicki, J., Olendrzynski, K., Jakobsen, H., and Berge, E.: EMEP Eulerian model for atmospheric transport and deposition of nitrogen species over Europe, *Environmental Pollution*, 102, 289 – 298, doi:10.1016/S0269-7491(98)80046-8, 1998.
- Karydis, V. A., Kumar, P., Barahona, D., Sokolik, I. N., and Nenes, A.: On the effect of dust particles
- 1125 on global cloud condensation nuclei and cloud droplet number, *Journal of Geophysical Research: Atmospheres*, 116, 204, doi:10.1029/2011JD016283, 2011.
- Knorr, W. and Heimann, M.: Impact of drought stress and other factors on seasonal land biosphere CO<sub>2</sub> exchange studied through an atmospheric tracer transport model, *Tellus B: Chemical and Physical Meteorology*, 47, 471–489, doi:10.3402/tellusb.v47i4.16062, 1995.
- 1130 Knoth, O. and Wolke, R.: An explicit-implicit numerical approach for atmospheric chemistry-transport modeling, *Atmospheric Environment*, 32, 1785 – 1797, doi:10.1016/S1352-2310(97)00476-7, 1998.
- Krämer, M., Rolf, C., Luebke, A., Afchine, A., Spelten, N., Costa, A., Meyer, J., Zöger, M., Smith, J., Herman, R. L., Buchholz, B., Ebert, V., Baumgardner, D., Borrmann, S., Klingebiel, M., and
- 1135 Avallone, L.: A microphysics guide to cirrus clouds – Part 1: Cirrus types, *Atmospheric Chemistry and Physics*, 16, 3463–3483, doi:10.5194/acp-16-3463-2016, 2016.
- Kärcher, B. and Lohmann, U.: A Parameterization of cirrus cloud formation: Homogeneous freezing including effects of aerosol size, *Journal of Geophysical Research: Atmospheres*, 107, AAC 9–1–



- AAC 9–10, doi:10.1029/2001JD001429, 2002.
- 1140 Kärcher, B. and Lohmann, U.: A parameterization of cirrus cloud formation: Heterogeneous freezing, *Journal of Geophysical Research: Atmospheres*, 108, doi:10.1029/2002JD003220, 2003.
- Köhler, C. H.: Optical properties of mineral dust aerosol in the thermal infrared, *AIP Conference Proceedings*, 1810, 050 001, doi:10.1063/1.4975513, 2017.
- Lee, S. S. and Penner, J. E.: Aerosol effects on ice clouds: can the traditional concept of aerosol indirect effects be applied to aerosol-cloud interactions in cirrus clouds?, *Atmospheric Chemistry and Physics*, 10, 10 345–10 358, doi:10.5194/acp-10-10345-2010, 2010.
- Lindner, T. H. and Li, J.: Parameterization of the Optical Properties for Water Clouds in the Infrared, *Journal of Climate*, 13, 1797–1805, doi:10.1175/1520-0442(2000)013<1797:POTOPF>2.0.CO;2, 2000.
- Luebke, A. E., Afchine, A., Costa, A., Grooß, J.-U., Meyer, J., Rolf, C., Spelten, N., Avallone, L. M.,  
1150 Baumgardner, D., and Krämer, M.: The origin of midlatitude ice clouds and the resulting influence on their microphysical properties, *Atmospheric Chemistry and Physics*, 16, 5793–5809, doi:10.5194/acp-16-5793-2016, 2016.
- Marcolli, C.: Deposition nucleation viewed as homogeneous or immersion freezing in pores and cavities, *Atmospheric Chemistry and Physics*, 14, 2071–2104, doi:10.5194/acp-14-2071-2014, 2014.
- 1155 Martcorena, B. and Bergametti, G.: Modeling the atmospheric dust cycle: 1. Design of a soil-derived dust emission scheme, *Journal of Geophysical Research: Atmospheres*, 100, 16 415–16 430, doi:10.1029/95JD00690, 1995.
- Meyer, J.: *Ice Crystal Measurements with the New Particle Spectrometer NIXE-CAPS*, <https://books.google.de/books?id=dSL6V0ZeDs0C>, 2013.
- 1160 Meyers, M. P., DeMott, P. J., and Cotton, W. R.: New Primary Ice-Nucleation Parameterizations in an Explicit Cloud Model, *Journal of Applied Meteorology*, 31, 708–721, doi:10.1175/1520-0450(1992)031<0708:NPINPI>2.0.CO;2, 1992.
- Mishchenko, M. I., Travis, L. D., and Lacis, A. A.: *Scattering, Absorption, and Emission of Light by Small Particles*, 2002.
- 1165 Mitchell, D. L., Lawson, R. P., and Baker, B.: Understanding effective diameter and its application to terrestrial radiation in ice clouds, *Atmospheric Chemistry and Physics*, 11, 3417–3429, <https://www.atmos-chem-phys.net/11/3417/2011/>, doi:10.5194/acp-11-3417-2011, 2011.
- Müller, T., Schladitz, A., Kandler, K., and Wiedensohler, A.: Spectral particle absorption coefficients, single scattering albedos and imaginary parts of refractive indices from ground based in situ measurements at Cape Verde Island during SAMUM-2, *Tellus B*, 63, 573–588, doi:10.1111/j.1600-0889.2011.00572.x, 2011.
- 1170 Niemand, M., Möhler, O., Vogel, B., Vogel, H., Hoose, C., Connolly, P., Klein, H., Bingemer, H., DeMott, P., Skrotzki, J., and Leisner, T.: A Particle-Surface-Area-Based Parameterization of Immersion Freezing on Desert Dust Particles, *Journal of the Atmospheric Sciences*, 69, 3077–3092, doi:10.1175/JAS-D-11-0249.1, 2012.
- O'Neill, N. T., Eck, T. F., Smirnov, A., Holben, B. N., and Thulasiraman, S.: Spectral discrimination of coarse and fine mode optical depth, *Journal of Geophysical Research: Atmospheres*, 108, doi:10.1029/2002JD002975, 2003.



- Ovtchinnikov, M. and Kogan, Y. L.: An Investigation of Ice Production Mechanisms in Small Cumuli-  
1180 form Clouds Using a 3D Model with Explicit Microphysics. Part I: Model Description, *Journal of  
the Atmospheric Sciences*, 57, 2989–3003, doi:10.1175/1520-0469(2000)057<2989:AIOIPM>2.0.CO;2,  
2000.
- Phillips, V. T. J., DeMott, P. J., and Andronache, C.: An Empirical Parameterization of Heterogeneous  
Ice Nucleation for Multiple Chemical Species of Aerosol, *Journal of the Atmospheric Sciences*, 65,  
1185 2757–2783, doi:10.1175/2007JAS2546.1, 2008.
- Prigent, C., Jimenez, C., and Catherinot, J.: Comparison of satellite microwave backscattering (AS-  
CAT) and visible/near-infrared reflectances (PARASOL) for the estimation of aeolian aerodynamic  
roughness length in arid and semi-arid regions, 5, 2933–2957, 2012.
- Pruppacher, H. and Klett, J.: *Microphysics of Clouds and Precipitation*, doi:10.1007/  
1190 978-0-306-48100-0, 2010.
- Rieger, D., Steiner, A., Bachmann, V., Gasch, P., Förstner, J., Deetz, K., Vogel, B., and Vogel, H.: Im-  
pact of the 4 April 2014 Saharan dust outbreak on the photovoltaic power generation in Germany,  
*Atmospheric Chemistry and Physics*, 17, 13 391–13 415, doi:10.5194/acp-17-13391-2017, 2017.
- Ritter, B. and Geleyn, J.-F.: A Comprehensive Radiation Scheme for Numerical Weather Prediction  
1195 Models with Potential Applications in Climate Simulations, *Monthly Weather Review*, 120, 303–  
325, doi:10.1175/1520-0493(1992)120<0303:ACRSFN>2.0.CO;2, 1992.
- Rose, T., Crewell, S., Löhnert, U., and Simmer, C.: A network suitable microwave radiome-  
ter for operational monitoring of the cloudy atmosphere, *Atmospheric Research*, 75, 183–200,  
doi:10.1016/j.atmosres.2004.12.005, 2005.
- 1200 Salvador, P., Alonso-Pérez, S., Pey, J., Artíñano, B., de Bustos, J. J., Alastuey, A., and Querol, X.:  
African dust outbreaks over the western Mediterranean Basin: 11-year characterization of atmo-  
spheric circulation patterns and dust source areas, *Atmospheric Chemistry and Physics*, 14, 6759–  
6775, doi:10.5194/acp-14-6759-2014, 2014.
- Saunders, R., Hocking, J., Turner, E., Rayer, P., Rundle, D., Brunel, P., Vidot, J., Rocquet, P., Matricardi,  
1205 M., Geer, A., Bormann, N., and Lupu, C.: An update on the RTTOV fast radiative transfer model  
(currently at version 12), *Geoscientific Model Development Discussions*, 2018, 1–32, doi:10.5194/  
gmd-2018-64, 2018.
- Schepanski, K., Heinold, B., and Tegen, I.: Harmattan, Saharan heat low, and West African monsoon  
circulation: modulations on the Saharan dust outflow towards the North Atlantic, *Atmospheric*  
1210 *Chemistry and Physics*, 17, 10 223–10 243, doi:10.5194/acp-17-10223-2017, 2017.
- Schumann, U., Graf, K., Bugliaro, L., Wirth, M., Ziereis, H., Giez, A., Jurkat, T., Kaufmann, S., Schlage,  
R., Zahn, A., Dörnbrack, A., Krämer, M., Minikin, A., and Voigt, C.: Contrail predictions for ML-  
CIRRUS – Method and Experiences, TAC4, Bad Kohlgrub, DLR FB 2015-38, 132-138. [http://elib.  
dlr.de/97373/](http://elib.dlr.de/97373/), 2016.
- 1215 Seifert, A. and Beheng, K. D.: A two-moment cloud microphysics parameterization for mixed-phase  
clouds. Part 1: Model description, *Meteorology and Atmospheric Physics*, 92, 45–66, doi:10.1007/  
s00703-005-0112-4, 2006.
- Seifert, P., Ansmann, A., Mattis, I., Wandinger, U., Tesche, M., Engelmann, R., Müller, D., Pérez, C.,



- and Hausteiner, K.: Saharan dust and heterogeneous ice formation: Eleven years of cloud observations at a central European EARLINET site, *Journal of Geophysical Research: Atmospheres*, 2010.
- 1220 Senf, F. and Deneke, H.: Uncertainties in synthetic Meteorol SEVIRI infrared brightness temperatures in the presence of cirrus clouds and implications for evaluation of cloud microphysics, *Atmospheric Research*, 183, 113 – 129, doi:10.1016/j.atmosres.2016.08.012, 2017.
- Shao, Y., Wyrwoll, K.-H., Chappell, A., Huang, J., Lin, Z., McTainsh, G. H., Mikami, M., Tanaka, T. Y.,  
1225 Wang, X., and Yoon, S.: Dust cycle: An emerging core theme in Earth system science, *Aeolian Research*, 2, 181 – 204, doi:10.1016/j.aeolia.2011.02.001, 2011.
- Shaw, R. A., Durant, A. J., and Mi, Y.: Heterogeneous Surface Crystallization Observed in Undercooled Water, *The Journal of Physical Chemistry B*, 109, 9865–9868, doi:10.1021/jp0506336, 2005.
- Sinyuk, A., Torres, O., and Dubovik, O.: Combined use of satellite and surface observations to infer  
1230 the imaginary part of refractive index of Saharan dust, *Geophysical Research Letters*, 30, 1081, doi:10.1029/2002GL016189, 2003.
- Smoydzin, L., Teller, A., Tost, H., Fnais, M., and Lelieveld, J.: Impact of mineral dust on cloud formation in a Saharan outflow region, *Atmospheric Chemistry and Physics*, 12, 11383–11393, doi:10.5194/acp-12-11383-2012, 2012.
- 1235 Tegen, I., Hollrig, P., Chin, M., Fung, I., Jacob, D., and Penner, J.: Contribution of different aerosol species to the global aerosol extinction optical thickness: Estimates from model results, *J. Geophys. Res.*, 102, 23895–23915, doi:10.1029/97JD01864, 1997.
- Tegen, I., Harrison, S. P., Kohfeld, K. I., Prentice, C., Coe, M., and Heimann, M.: Impact of vegetation and preferential source areas on global dust aerosol: Results from a model study, *Journal of Geophysical Research: Atmospheres*, 107, AAC 14–1–AAC 14–27, doi:10.1029/2001JD000963,  
1240 2002.
- Tucker, C. J., Pinzon, J. E., Brown, M. E., Slayback, D. A., Pak, E. W., Mahoney, R., Vermote, E. F., and Saleous, N. E.: An extended AVHRR 8-km NDVI dataset compatible with MODIS and SPOT vegetation NDVI data, *International Journal of Remote Sensing*, 26, 4485–4498, doi:10.1080/01431160500168686, 2005.
- 1245 Ullrich, R., Hoose, C., Möhler, O., Niemand, M., Wagner, R., Hhler, K., Hiranuma, N., Saathoff, H., and Leisner, T.: A New Ice Nucleation Active Site Parameterization for Desert Dust and Soot, *Journal of the Atmospheric Sciences*, 74, 699–717, doi:10.1175/JAS-D-16-0074.1, 2017.
- Verheggen, B., Cozic, J., Weingartner, E., Bower, K., Mertes, S., Connolly, P., Gallagher, M., Flynn, M., Choulaton, T., and Baltensperger, U.: Aerosol partitioning between the interstitial and the condensed phase in mixed-phase clouds, *Journal of Geophysical Research: Atmospheres*, 112, 202, doi:10.1029/2007JD008714, 2007.
- 1250 Voigt, C., Schumann, U., Minikin, A., Abdelmonem, A., Afchine, A., Borrmann, S., Boettcher, M., Buchholz, B., Bugliaro, L., Costa, A., Curtius, J., Dollner, M., Dörnbrack, A., Dreiling, V., Ebert, V., Ehrlich, A., Fix, A., Forster, L., Frank, F., Fütterer, D., Giez, A., Graf, K., Groß, J.-U., Groß, S., Heimerl, K., Heinold, B., Hüneke, T., Järvinen, E., Jurkat, T., Kaufmann, S., Kenntner, M., Klingebiel, M., Klimach, T., Kohl, R., Krämer, M., Krisna, T. C., Luebke, A., Mayer, B., Mertes, S., Molleker, S., Petzold, A., Pfeilsticker, K., Port, M., Rapp, M., Reutter, P., Rolf, C., Rose, D., Sauer, D., Schäfler,



- A., Schlage, R., Schnaiter, M., Schneider, J., Spelten, N., Spichtinger, P., Stock, P., Walser, A., Weigel, R., Weinzierl, B., Wendisch, M., Werner, F., Wernli, H., Wirth, M., Zahn, A., Ziereis, H., and Zöger, M.: ML-CIRRUS: The Airborne Experiment on Natural Cirrus and Contrail Cirrus with the High-Altitude Long-Range Research Aircraft HALO, *Bulletin of the American Meteorological Society*, 98, 271–288, doi:10.1175/BAMS-D-15-00213.1, 2017.
- 1260 Wagner, R., Bunz, H., Linke, C., Möhler, O., Naumann, K.-H., Saathoff, H., Schnaiter, M., and Schurath, U.: Chamber Simulations of Cloud Chemistry: The AIDA Chamber, pp. 67–82, doi:10.1007/1-4020-4232-9\_5, 2006.
- Wang, H., Shi, G., Zhu, J., Chen, B., Che, H., and Zhao, T.: Case study of longwave contribution to dust radiative effects over East Asia, *Chinese Science Bulletin*, 58, 3673–3681, doi:10.1007/s11434-013-5752-z, 2013.
- 1265 Weigel, R., Spichtinger, P., Mahnke, C., Klingebiel, M., Afchine, A., Petzold, A., Krämer, M., Costa, A., Molleker, S., Reutter, P., Szakáll, M., Port, M., Grulich, L., Jurkat, T., Minikin, A., and Borrmann, S.: Thermodynamic correction of particle concentrations measured by underwing probes on fast-flying aircraft, *Atmospheric Measurement Techniques*, 9, 5135–5162, doi:10.5194/amt-9-5135-2016, 2016.
- Wolke, R., Knoth, O., and Münzenberg-St.Denis, A.: Online Coupling of Multiscale Chemistry-Transport Models with Non-Hydrostatic Meteorological Models, pp. 769–770, doi:10.1007/978-1-4615-4153-0\_98, 2000.
- 1275 Wolke, R., Knoth, O., Hellmuth, O., Schröder, W., and Renner, E.: The parallel model system LM-MUSCAT for chemistry-transport simulations: Coupling scheme, parallelization and applications, 13, 363 – 369, doi:10.1016/S0927-5452(04)80048-0, 2004.
- Wolke, R., Schröder, W., Schrödner, R., and Renner, E.: Influence of grid resolution and meteorological forcing on simulated European air quality: A sensitivity study with the modeling system COSMO-MUSCAT, *Atmospheric Environment*, 53, 110 – 130, doi:doi.org/10.1016/j.atmosenv.2012.02.085, 2012.
- 1280 Zhang, D., Wang, Z., Kollias, P., Vogelmann, A., Yang, K., and Luo, T.: Ice particle production in mid-level stratiform mixed-phase clouds observed with collocated A-Train measurements, *Atmospheric Chemistry and Physics*, 18, 4317–4327, doi:10.5194/acp-18-4317-2018, 2018.
- Zhang, L., Gong, S., Padro, J., and Barrie, L.: A size-segregated particle dry deposition scheme for an atmospheric aerosol module, *Atmospheric Environment*, 35, 549 – 560, doi:doi.org/10.1016/S1352-2310(00)00326-5, 2001.
- 1290 Zhao, B., Gu, Y., Liou, K., Wang, Y., Liu, X., Huang, L., Jiang, J. H., and Su, H.: Type-Dependent Responses of Ice Cloud Properties to Aerosols From Satellite Retrievals, *Geophysical Research Letters*, 45, 3297–3306, doi:10.1002/2018GL077261, 2018.



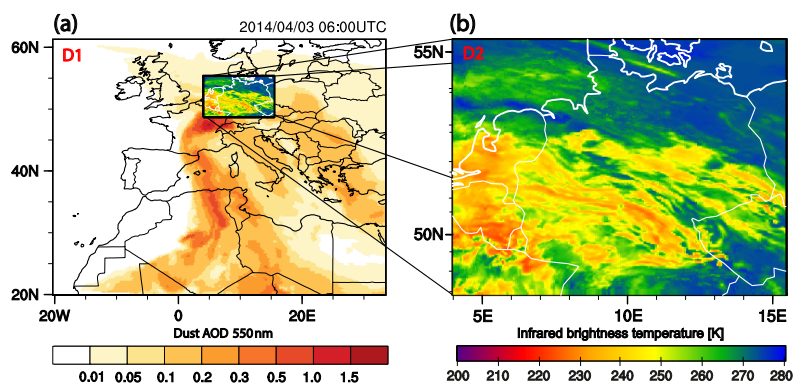


Fig. 1. (a) Model simulation domain D1 with 14km grid spacing showing dust AOD fields by COSMO-MUSCAT. (b) Inner model domain D2 with 2.8 km grid spacing showing simulated infrared brightness temperatures of a COSMO-MUSCAT run with interactive dust effects on cloud microphysics.

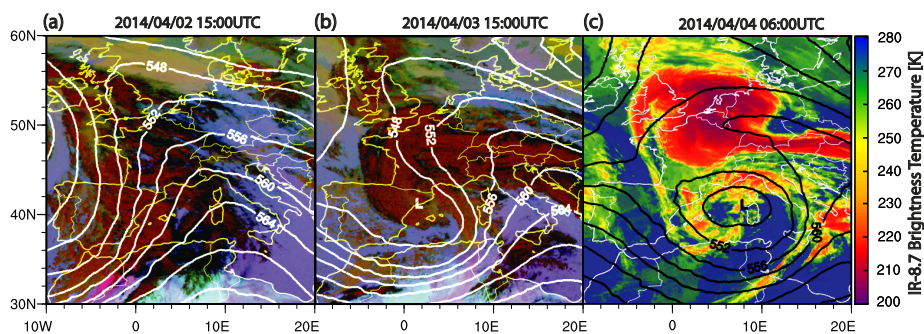
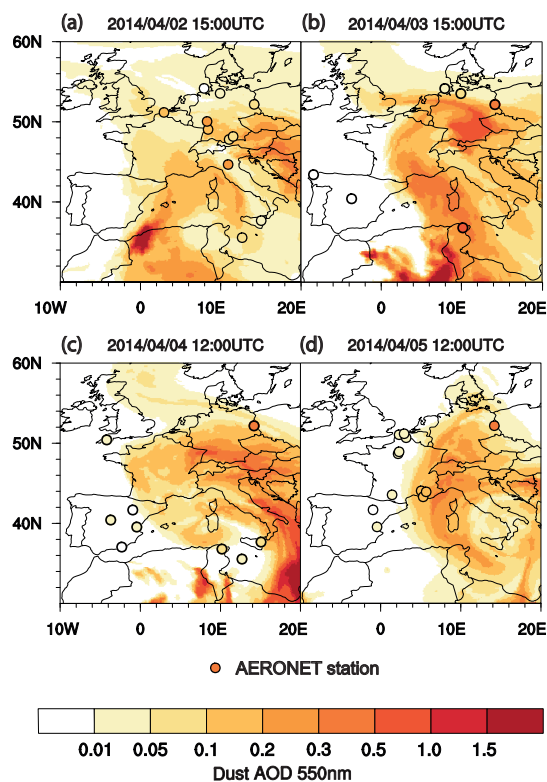
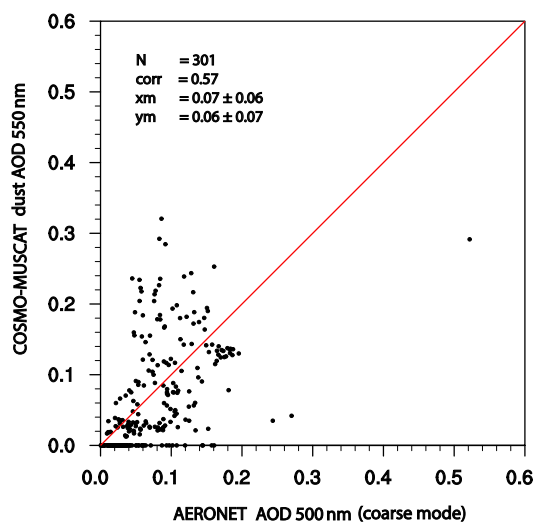


Fig. 2. (a, b) Meteosat Second Generation (MSG) SEVIRI dust composite images for 2 April, 15:00 UTC and 3 April, 15:00 UTC, respectively. (c) MSG SEVIRI IR-8.7 brightness temperature for 4 April, 06:00 UTC. All images are overlaid with 500 hPa geopotential height contour lines from COSMO-MUSCAT (14 km) with 4 dam spacing.





**Fig. 3.** Maps of dust AOD at 550 nm as simulated with the dust transport model COSMO-MUSCAT on the D1 grid for the dates 2 April, 15:00 UTC, 3 April, 15:00 UTC, 4 April 12:00 UTC, and 5 April, 12:00 UTC, respectively. AERONET observations of coarse mode AOD at 500 nm are marked by coloured circles.



**Fig. 4.** Scatter plot of observed 500 nm coarse-mode AOD and modeled dust AOD from the 14 km COSMO-MUSCAT run for all available AERONET stations within domain D1 (see Fig. 1). The data pool was gathered over the period from 2 April, 00:00 UTC to 6 April, 00:00 UTC by taking hourly model outputs and AERONET observations available within  $\pm 0.5$  h of corresponding time frames into account. Parameters printed are number of data points in each set (N), correlation coefficient between both data sets (corr), mean of the observations (xm), and mean of modeled values (ym).

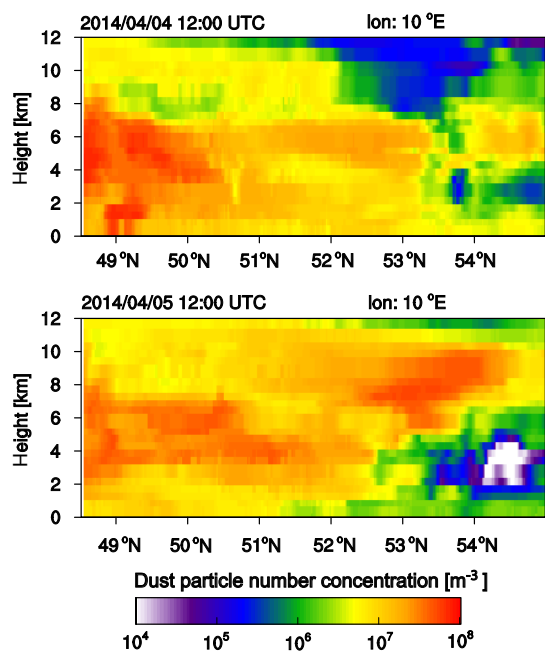


Fig. 5. Vertical cross section of dust particle number concentration along the meridian  $10^\circ\text{E}$  over Germany as computed with COSMO-MUSCAT at 2.8 km horizontal resolution for 4 and 5 April 2014 at 12:00 UTC respectively.

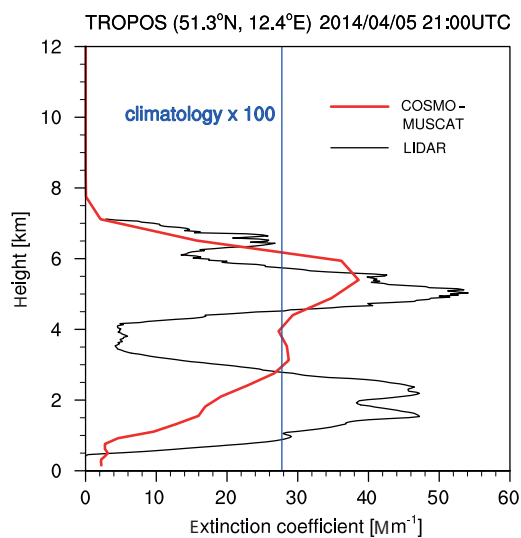


Fig. 6. Vertical profile of aerosol extinction coefficient retrieved from lidar observations obtained at TROPOS in Leipzig on 5 April, 21:00 UTC, and calculated from the modeled dust fields at the nearest grid point.

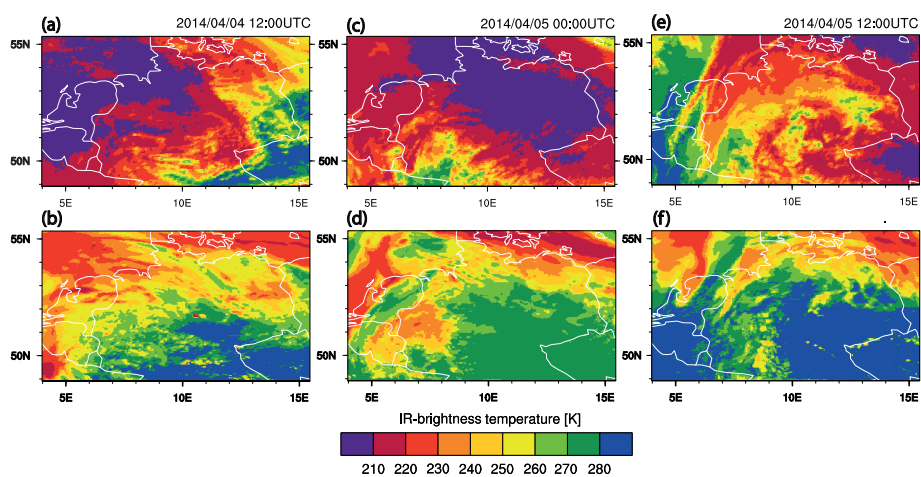


Fig. 7. Infrared (IR; 8.7  $\mu\text{m}$  channel) brightness temperature maps based on (top row) MSG SEVIRI data of EUMETSAT (top row) and (bottom row) on the infrared simulation with the model output fields of the run SMLBK. Areas of brightness temperatures below 240 K are colored.

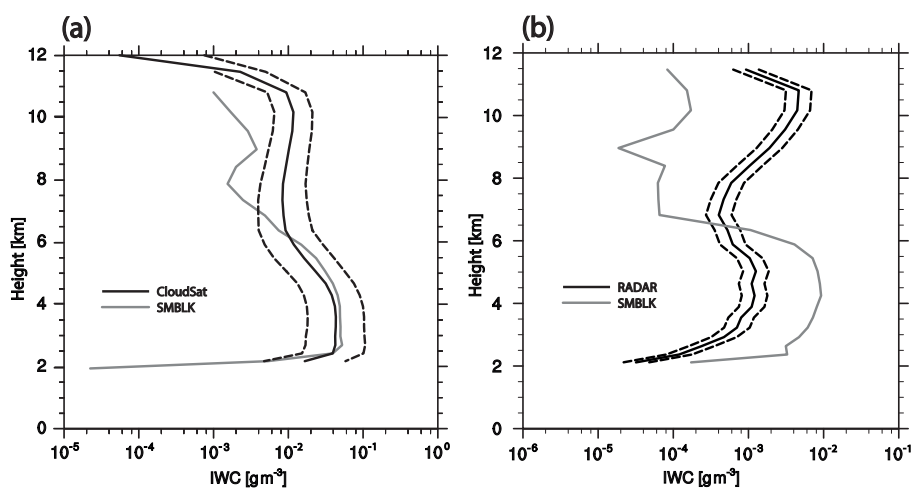
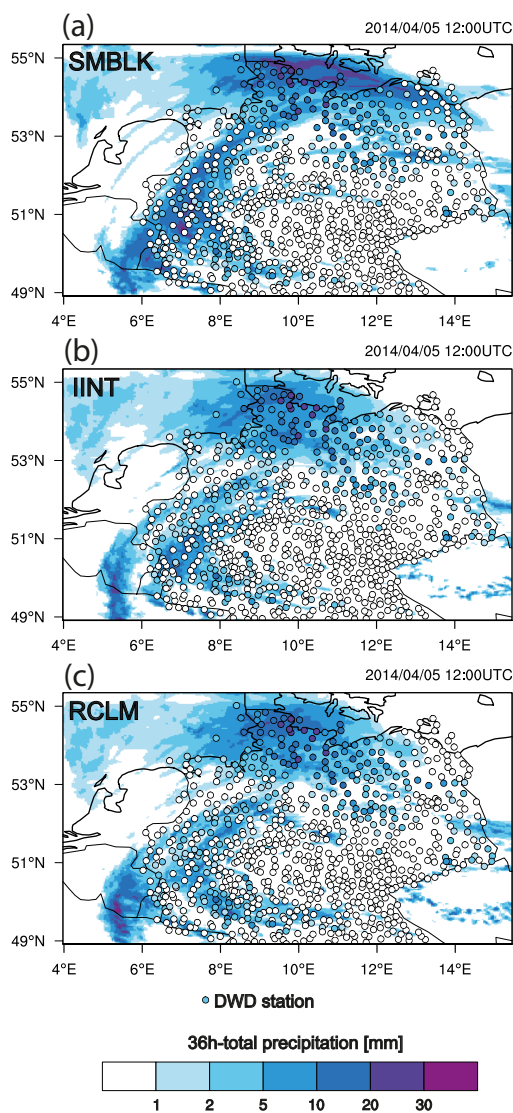


Fig. 8. (a) Spatially averaged vertical profiles of IWC retrieved from cloud radar and the model run SMBLK along the CloudSat satellite overpass on 4 April, 12:30 UTC. (b) Similar to (a), but for the time averaged radar observations and model data at the TROPOS site in Leipzig (51.3 ° N, 12.3 ° E). Absolute values are depicted by full lines, while dashed lines mark the averaged measurement uncertainty of cloud radar retrievals.



**Fig. 9.** Maps of modeled 36 h-precipitation totals for the different sensitivity model runs (a) SMBLK, (b) IINT, and (c) RCLM overlaid with station precipitation measurements (black rendered, colored circles) from DWD stations.

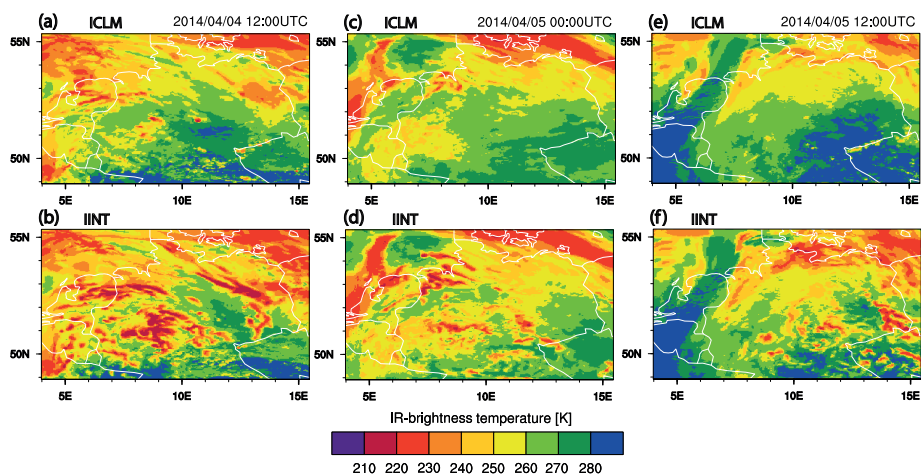


Fig. 10. Simulated infrared images of brightness temperature as in Fig. 7 for (top row) the run with climatological mean dust interactions (ICLM) and (bottom row) interactive dust effects (IINT). Areas of brightness temperatures below 240 K are colored.

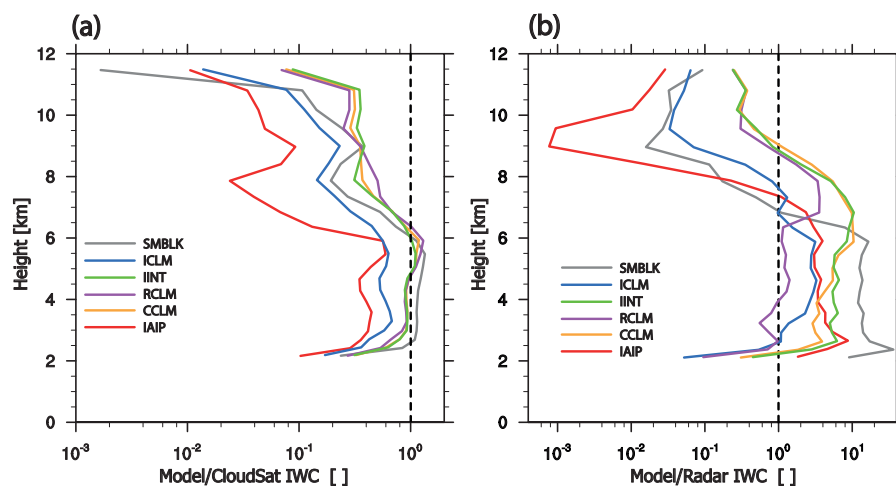


Fig. 11. Vertical profiles of model-measurement ratios of IWC for (a) the CloudSat overpass on 4 April, 12:00 UTC and (b) for the time averaged radar observations at TROPOS site in Leipzig (51.3 ° N, 12.3 ° E).



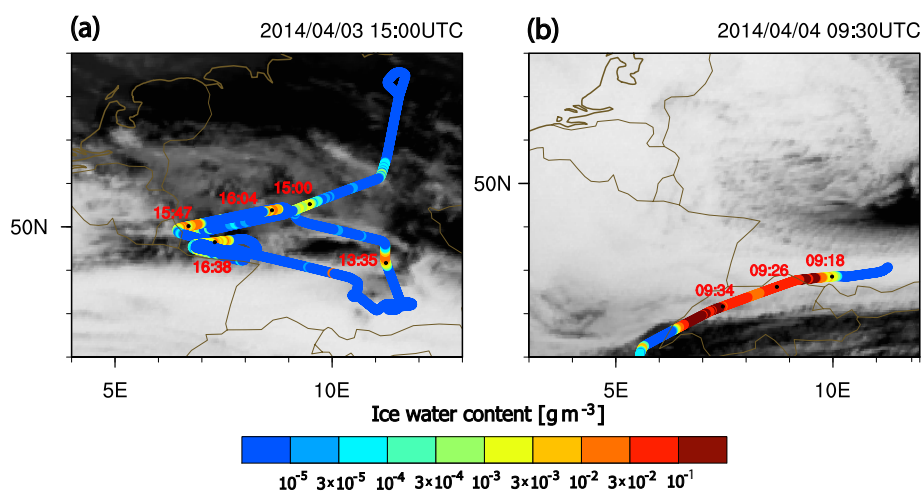


Fig. 12. Trajectories of ML-CIRRUS flights conducted (a) on 3 April and (b) on 4 April respectively. The colors of the trajectories represent IWC above 7 km altitude, which is inferred from the measured ice PSD. In addition, flight time stamps in UTC are shown for both tracks. The background shows MSG SEVIRI IR-8.7 images from (a) on 3 April, 15:00 UTC and (b) on 4 April, 09:00 UTC respectively, indicating differences in cloud cover with cirrus on these days.

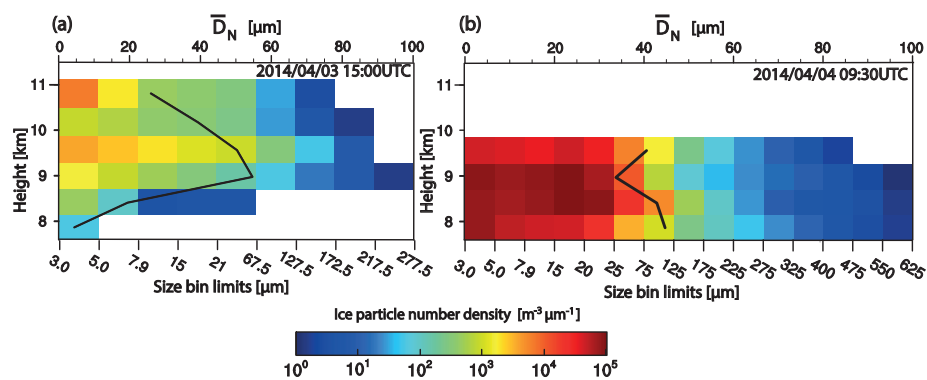


Fig. 13. Ice PSD from measurements aboard HALO aircraft during ML-CIRRUS campaign on (a) 3 April 15:00 UTC and (b) on 4 April 09:30 UTC. The area plots show vertical profiles of measured particle number density  $dn_i/dd$  for the size bins (limits marked by the ticks of bottom x-axis) and interpolated to the 2.8 km COSMO-MUSCAT vertical levels. In addition for each layer, the number weighted volume mean particle diameter  $\bar{D}_N$  is shown for measurements (top x-axis).

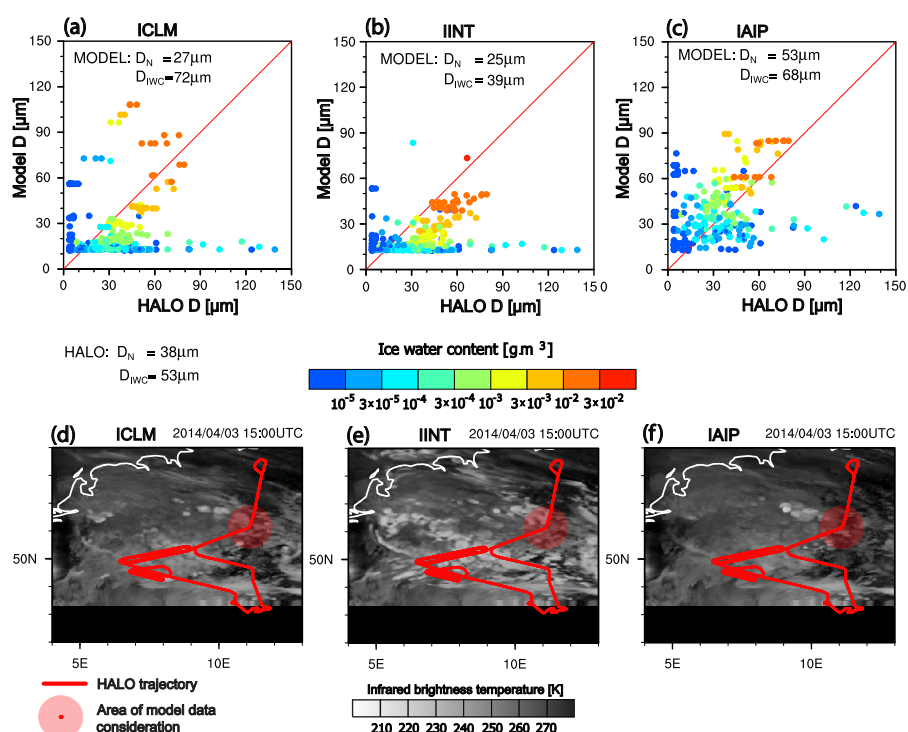


Fig. 14. (a, b, c) Scatter plots of ice particle diameter  $D_i$  measured aboard HALO during ML-CIRRUS against model results for the model runs ICLM, IINT and IAIP, respectively.  $\bar{D}_N$  is the number-weighted average of  $D_i$ ,  $\bar{D}_{IWC}$  is the IWC-weighted average of  $D_i$ . (d, e, f) Simulated infrared images for model runs ICLM, IINT and IAIP overlaid with HALO flight track and a reddish shaded circle, within which model data are considered for the comparison.

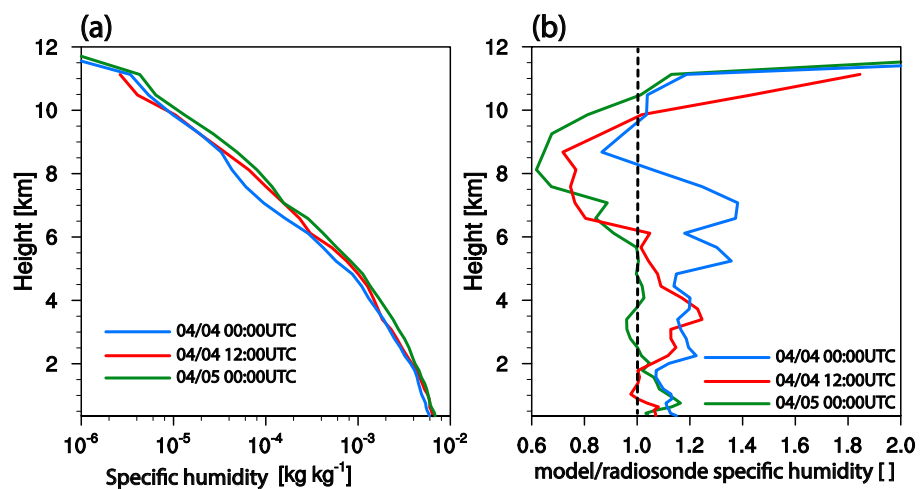


Fig. 15. (a) Averaged vertical profiles of specific humidity (SH) obtained from atmospheric sounding at all stations located within the domain D2 for the dates 4 April, 00:00 UTC, 4 April, 12:00 UTC, and 5 April, 00:00 UTC, respectively. (b) Averaged model-measurement ratios of SH as in (a).